Remote Sensing of Environment 196 (2017) 113–133

Contents lists available at ScienceDirect

Remote Sensing of Environment

journal homepage: www.elsevier.com/locate/rse

A Fully Automated Supraglacial lake area and volume Tracking ("FAST") algorithm: Development and application using MODIS imagery of West Greenland

Andrew G. Williamson *, Neil S. Arnold, Alison F. Banwell, Ian C. Willis

Scott Polar Research Institute, University of Cambridge, Cambridge, UK

ARTICLE INFO

Article history:
Received 14 November 2016
Received in revised form 26 April 2017
Accepted 28 April 2017
Available online 9 May 2017

Keywords:
Supraglacial lakes
Supraglacial lake tracking
Supraglacial hydrology
Supraglacial lake drainage
Automated methodology
Greenland Ice Sheet
Satellite imagery
MODIS
Landsat-8 OLI
Store Glacier
Paakitsoq

ABSTRACT

Supraglacial lakes (SGLs) on the Greenland Ice Sheet (GrIS) influence ice dynamics if they drain rapidly by hydrofracture. MODIS data are often used to investigate SGLs, including calculating SGL area changes through time, but no existing work presents a method that tracks changes to individual (and total) SGL volume in MODIS imagery over a melt season. Here, we develop such a method by first testing three automated approaches to derive SGL areas from MODIS images from the MOD09 level-2 surface-reflectance product, by comparing calculated areas for the Paakitsoq and Store Glacier regions in West Greenland with areas derived from Landsat-8 (LS8) images. Second, we apply a physically-based depth-calculation algorithm to the pixels within the SGL boundaries from the best performing area-derivation method, and compare the resultant depths with those calculated using the same method applied to LS8 imagery. Our results indicate that SGL areas are most accurately generated using dynamic thresholding of MODIS band 1 (red) MOD09 data with a 0.640 threshold value; calculated values from MODIS are closely comparable to those derived from LS8. Third, we incorporate the best performing area- and depth-detection methods into a Fully Automated SGL Tracking ("FAST") algorithm that tracks individual SGLs between successive MODIS images. Finally, we apply the FAST algorithm to the two study regions, where it identifies 43 (Paakitsoq) and 19 (Store Glacier) rapidly draining SGLs during 2014, representing 21% and 15% of the respective total SGL populations, including some clusters of rapidly draining SGLs. The FAST algorithm improves upon existing automatic SGL tracking methods through its calculation of both SGL areas and volumes over large regions of the GrIS on a fully automatic basis. It therefore has the potential to be used for investigating statistical relationships between SGL areas, volumes and drainage events over the whole of the GrIS, and over multiple seasons, which might provide further insights into the factors that trigger rapid SGL drainage.

1. Introduction

The Greenland Ice Sheet (GrIS) is losing mass at an accelerating rate, which is predicted to continue for at least the coming century; developing a robust understanding of the processes contributing to this mass loss forms a fundamental research agenda (Rignot et al., 2011; Vaughan et al., 2013; van den Broeke et al., 2016; Noël et al., 2016). Supraglacial lakes (SGLs) that form annually in the ablation zone in the early to mid-melt season contribute to the GrIS's negative mass balance in two main ways. First, they influence surface melt rates, particularly through their effect on lowering albedo (Lüthje et al., 2006; Tedesco and Steiner, 2011; Tedesco et al., 2012). Second, they affect ice-dynamic processes, since their rapid drainage by hydrofracture allows large pulses of surface meltwater to reach the GrIS's bed, which may impact subglacial effective pressures, raising basal water pressures and hence surface ice velocities (Zwally et al., 2002; Alley et al., 2005; Shepherd et al., 2009; Bartholomew et al., 2010, 2011a, 2011b, 2012; Schoof, 2010; Sundal et al., 2011; Hoffman et al., 2011; Colgan et al., 2011a; Cowton et al., 2013; Joughin et al., 2013; Sole et al., 2013; Tedstone et al., 2013; Andrews et al., 2014; Bougamont et al., 2014; Dow et al., 2015; Stevens et al., 2015). This process is of particular concern since over 200 rapid SGL drainages are thought to occur annually across the GrIS, affecting ~10% of the total SGL population (Selmes et al., 2011). Hydrofracture also opens up moulins that can continue delivering meltwater to the bed throughout the remainder of the melt season, influencing basal water pressures and sliding over longer timescales (Palmer et al., 2011; Colgan et al., 2011b; Sole et al., 2013; Banwell et al., 2013, 2016; Tedstone et al., 2014).

Satellite-based remote sensing is a common approach for investigating the locations of SGLs, and their filling and drainage patterns, and has proven useful to help reduce the uncertainties surrounding the current

* Corresponding author.
E-mail address: agw41@cam.ac.uk (A.G. Williamson).

http://dx.doi.org/10.1016/j.rse.2017.04.032

state and future evolution of the GrIS's hydrological system. However, remote techniques face a compromise between data with high spatial but low temporal resolution, and vice versa. Optical imagery from the relatively high-resolution Landsat (30 m) and Advanced Spaceborne Thermal Emission and Reflection Radiometer (ASTER; 15 m) satellites has been employed to track SGL filling and draining at high spatial resolution (Sneed and Hamilton, 2007; McMillan et al., 2007; Georgiou et al., 2009; Banwell et al., 2014; Arnold et al., 2014; Legleiter et al., 2014; Pope et al., 2016; Moussavi et al., 2016; Miles et al., 2016; Langley et al., 2016). But, since rapid SGL drainage events may occur in as little as two hours (Das et al., 2008), and typically within 24–96 h (Selmes et al., 2011), the precise timing and duration of such events cannot be identified with Landsat or ASTER because repeat imaging times are often at best ~4 d, and are sometimes considerably longer due to the sensor's orbital geometry and site-specific cloud cover. To better pinpoint the timing and duration of rapid drainage, daily MODerate-resolution Imaging Spectroradiometer (MODIS) data have been used (Box and Ski, 2007; Sundal et al., 2009; Selmes et al., 2011, 2013; Liang et al., 2012; Johansson and Brown, 2013; Johansson et al., 2013; Morriss et al., 2013; Fitzpatrick et al., 2014; Everett et al., 2016), but with MODIS's lower spatial resolution (~250–500 m), SGLs under two pixels in area (~0.125 km^2) cannot confidently be resolved.

Several methods have been used to calculate SGL areas from MODIS data; however, a consensus on the best technique to use has not yet emerged. To date, only one study (Leeson et al., 2013) examines the relative performance of some of these algorithms. In addition, although MODIS images are commonly used to calculate SGL areas, SGL depths and volumes are rarely calculated and, if they are, they are usually derived from empirical depth-reflectance techniques (Box and Ski, 2007; Fitzpatrick et al., 2014) or first-order area-volume scaling relationships (Liang et al., 2012; Morriss et al., 2013), rather than from physically-based methods (Morriss et al., 2013; Ignéczi et al., 2016). This limitation has made it difficult to use MODIS imagery to calculate the magnitudes of water delivery through hydrofracture to the bed from rapid SGL drainage events.

The overall objective of our study is to address the shortfalls mentioned above by developing and applying a Fully Automated SGL Tracking ("FAST") algorithm, which is capable of generating time-dependent SGL areas and, for the first time, volumes from successive MODIS images. We divide this objective into four aims. First, we extend the existing work that assesses and validates algorithms employed to calculate SGL areas automatically from MODIS imagery. For this, we compare SGL areas derived using three automatic methods applied to MODIS with SGL areas derived from higher-resolution Landsat-8 (LS8) imagery. This first step is crucial since we require accurate SGL boundaries to use as one of the input datasets for the SGL depth and volume calculations. Second, we link the best SGL area-calculation technique to a physically-based approach for estimating MODIS SGL depths and volumes, and validate these data against values calculated from LS8 images. Third, we incorporate the most effective SGL area- and depth-calculation methods into the FAST algorithm, which tracks the area and volume evolution of all individual SGLs within a series of MODIS images. Finally, once we have developed and tested the FAST algorithm, we use it to investigate the incidence of rapid SGL drainage events within two sectors of West Greenland (Fig. 1): (a) the Paakitsoq region, a land-terminating sector, north of Jakobshavn Isbræ; and (b) the region surrounding Store Glacier, a large, fast-flowing marine-terminating outlet in the Uummannaq district, north of the Paakitsoq region.

2. Previous approaches to derive supraglacial lake properties

This section presents a brief overview of existing research methods to measure SGL area and depth from the images collected by various satellite sensors. In Sections 2.1.1 to 2.1.3, we outline the three area-derivation methods that are tested within our research reported later; Section 2.1.4 presents a briefer summary of less frequently used methods that are not examined in our study; and Sections 2.1.5 outlines the methods used to appraise SGL area-derivation techniques to provide context for the appraisal conducted under the first aim of our study. Finally, Section 2.2 gives details about the physically-based method used within our work.

2.1. Supraglacial lake area

2.1.1. Static band thresholding

SGL boundaries are sometimes delimited manually (e.g. McMillan et al., 2007; Lampkin, 2011; Lampkin and VanderBerg, 2011; Hoffman et al., 2011; Langley et al., 2016) but this is time-consuming and subject to user bias, so automatic methods are frequently preferred. One method for calculating SGL areas, proposed by Box and Ski (2007) for MODIS, uses a ratio of the blue (band 3) to red (band 1) surface-reflectance values, with a threshold value (which may require lake-by-lake adjustment) chosen to define the water-covered pixels in a scene. This approach functions on the principle that red wavelengths are attenuated more strongly than blue ones within water columns, reducing red reflectance values compared to blue ones. Thus, the ratio of blue to red reflectance can help to identify water-covered pixels. This method has been applied successfully to Landsat scenes (e.g. Banwell et al., 2014; Arnold et al., 2014; Pope et al., 2016), and has also informed fuzzy-logic-based image classifications for SGL identification (Sundal et al., 2009).

2.1.2. The Normalised Difference Water Index

The Normalised Difference Water Index (NDWI) also employs the red and blue bands to derive SGL areas, and is defined as:

$$\mathrm{NDWI} = \frac{(\text{blue band reflectance} - \text{red band reflectance})}{(\text{blue band reflectance} + \text{red band reflectance})}. \quad (1)$$

A threshold NDWI value is needed to define water-covered pixels, with tuning required depending upon the site of interest (Huggel et al., 2002; Xu, 2006; Morriss et al., 2013; Doyle et al., 2013; Yang and Smith, 2013; Moussavi et al., 2016; Miles et al., 2017). Many glaciological studies use the NDWI (occasionally with modification to include, for example, the near-infrared and green bands) for MODIS imagery (Morriss et al., 2013; Doyle et al., 2013; Fitzpatrick et al., 2014), and for other sensors, notably Landsat and WorldView-2 (Huggel et al., 2002; Xu, 2006; Gardelle et al., 2011; Yang and Smith, 2013; Moussavi et al., 2016; Miles et al., 2017; Miles et al., in review). The NDWI's performance can be improved to minimise SGL misclassification through first isolating image pixels that satisfy certain surface-reflectance criteria, such as a requirement for a high (or low) reflectance value in the blue (or red) band (Fitzpatrick et al., 2014).

2.1.3. Dynamic band thresholding

An alternative approach first proposed by Selmes et al. (2011) is dynamic thresholding of the red band, which has been used subsequently by Selmes et al. (2013) and Everett et al. (2016). Similar to the static blue/red band thresholding approach, this method also exploits the pronounced attenuation of red light within a water column, and compares a central pixel's red reflectance against the mean of the red reflectance for all 441 pixels within a moving 21-by-21 pixel window surrounding this pixel. SGLs are defined as all locations where the central pixel's reflectance is below a given threshold, such as 0.65 of the mean reflectance within the window (Selmes et al., 2011). This effectively gives this approach a dynamic spatial variability since the background reflectance within the moving window changes spatially across the GrIS. This technique has not been applied to the other visible MODIS bands because they would need sharpening to 250 m resolution, causing loss of fidelity in the original data (Selmes, 2011).

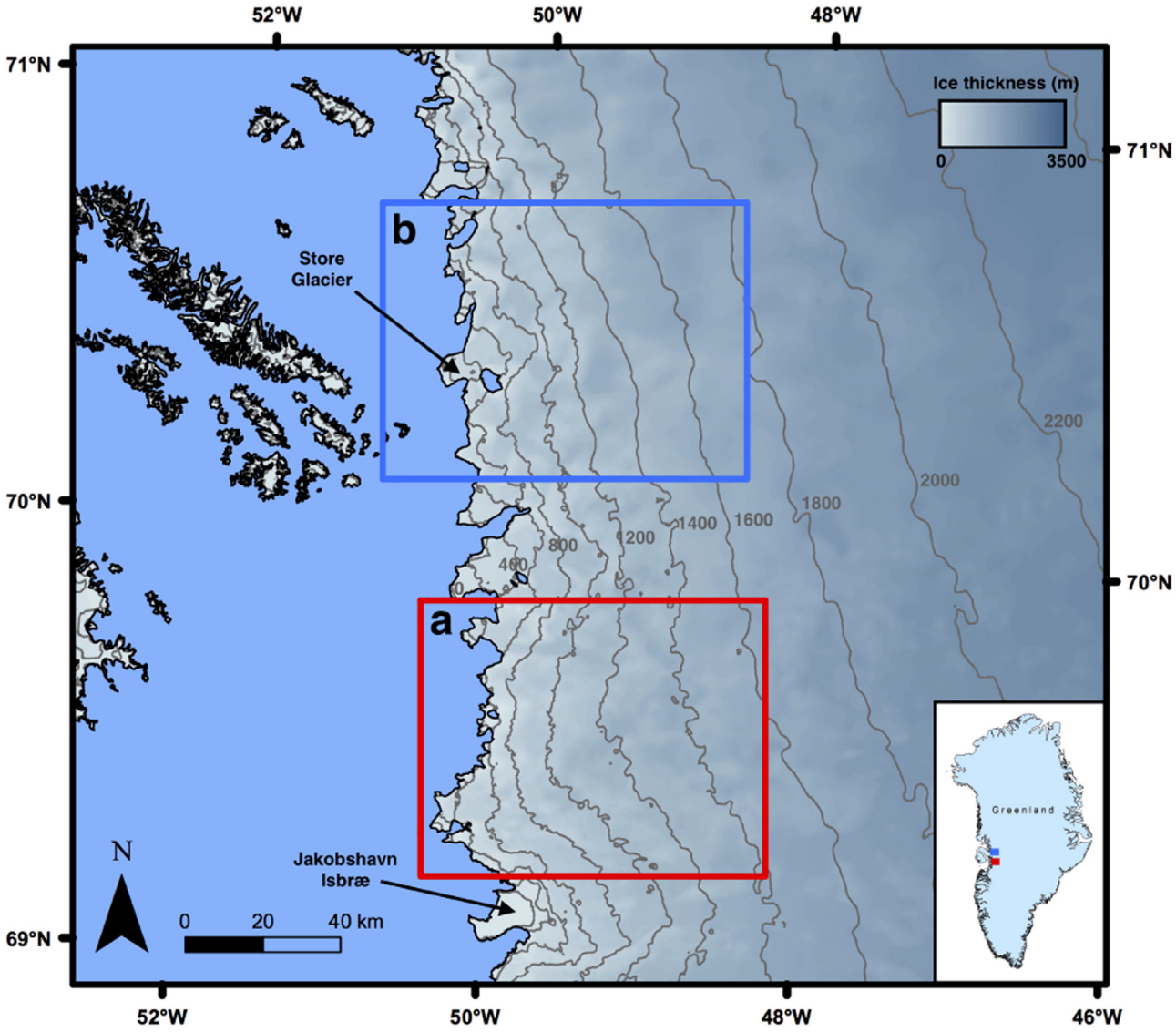

Fig. 1. Study sites in West Greenland: (a) the Paakitsoq region delineated by the red box; and (b) the Store Glacier region within the blue box. The grey background shading represents ice thickness (m), and the grey contour lines depict ice-surface elevation (m above sea level). The black line within the boxes for the study regions delineates the GrIS margin. The inset shows the location of sites (a) and (b) within Greenland.

2.1.4. Other approaches

Various other methods have also been used to derive SGL areas from remotely sensed imagery. First, image histograms can be automatically classified with the use of a spatially dynamic window that moves across images; these histograms display different characteristics based upon whether an image has SGLs present (Liang et al., 2012; Howat et al., 2013). Second, images can be segmented, with bimodal histograms created based upon buffered regions around SGLs, which are then examined dynamically to accurately identify SGL boundaries (Yang et al., 2015; Yang and Smith, 2016). Third, fuzzy-logic membership can explore the likelihood that an image pixel fits within a specific class (Sundal et al., 2009). Fourth, object-oriented classification can determine descriptive quantities about groups of pixels (Johansson and Brown, 2013). Finally, textural analysis employs the spectral signatures for scenes and identifies SGLs based on a maximum-likelihood algorithm (Lettang et al., 2013).

2.1.5. Appraisal of supraglacial lake area-calculation techniques

Studies calculating SGL areas using MODIS imagery normally assess the performance of their methods through validation with higher spatial resolution imagery from another multispectral sensor, typically Landsat or ASTER. Despite several studies conducting independent validations, only one (Leeson et al., 2013) evaluates the performance of several SGL area-derivation techniques for MODIS imagery by comparing them against a single validation dataset, and no single consensus has emerged regarding the best technique to use. Leeson et al. (2013) evaluated the methods of Sundal et al. (2009), Selmes et al. (2011), and Johansson and Brown (2013) for the Russell Glacier region, West Greenland. The different methods' performance was assessed by comparing the number and size of SGLs reported using each algorithm with those delineated manually from MODIS imagery and corresponding ASTER scenes. Each method underestimated the total number of SGLs (when compared with the number delimited manually) to a differing degree, leading to the recommendation that all methods should be combined to identify the maximum number of SGLs within a specific region (Leeson et al., 2013). Although Selmes et al.'s (2011) method reported the fewest SGLs overall — 52% of manually delineated SGLs — it calculated SGL area most accurately, with a 0.48 km^2 root mean square error (RMSE), compared with 0.78 km^2 and 0.95 km^2 RMSEs for Sundal et al.'s (2009) and Johansson and Brown's (2013) techniques, respectively. Leeson et al. (2013) indicated that the low number of SGLs

derived from Selmes et al.'s (2011) approach likely resulted from the *a priori* SGL distribution required as an input to that technique. The first aim of this research involves extending this limited range of appraisal work to determine which of the three techniques described in Sections 2.1.1 to 2.1.3 is best to incorporate into a fully automated SGL area-derivation algorithm.

2.2. Supraglacial lake depth and volume

2.2.1. Empirically-based approaches

Although MODIS imagery has been widely used to calculate SGL areas, it has been used far less frequently to calculate SGL pixel depths, and thus SGL volumes. Most of the studies that have conducted this analysis employ either a first-order relationship between SGL areas and volumes by approximating SGL basins as cones (Liang et al., 2012), use areas as proxies for volumes (Morriss et al., 2013), or use empirically-derived depth-reflectance curves from field data to calculate pixel depths, which are integrated to provide SGL volumes (e.g. Box and Ski, 2007; Fitzpatrick et al., 2014). While helpful for deriving information on changes to SGL volume for specific sectors of the GrIS in individual years, these methods lack a physical basis, so they cannot necessarily be applied with confidence to other regions of the GrIS or to different years.

2.2.2. A physically-based approach

Sneed and Hamilton (2007), after Philpot (1989), developed the first physically-based (i.e. radiative transfer) water-depth retrieval algorithm for SGLs, which they applied to ASTER data. The method is based on the attenuation of light within a water column according to the Bouguer-Lambert-Beer law; deeper water results in higher light attenuation within the column than shallower water. This phenomenon is observed for all wavelengths of visible light, but the attenuation rate varies by wavelength. To apply this to satellite imagery, therefore, the waveband experiencing the greatest change in attenuation over the expected water depth range needs to be selected. The attenuation rate can be used in the calculation of water depth (z, in m) if certain other properties of SGLs and the images are known:

$$z = \frac{\left[\ln\left(A_d - R_\infty\right) - \ln\left(R_{pix} - R_\infty\right)\right]}{g}, \quad (2)$$

where A_d is the SGL bottom albedo, R_∞ is the reflectance for optically deep (>40 m) water, R_{pix} is the reflectance of a pixel of interest, and g describes the losses in upward and downward travel in a water column. Since the method is physically based, it does not require site-specific tuning, meaning that it can be widely applied across the GrIS, with the option to test the sensitivity to its physical parameters (e.g. Pope et al., 2016). Pope et al. (2016) fully describe the assumptions inherent in this method, but, briefly, these are that: (i) the SGL surface is not disturbed by wind; (ii) the SGL bottom is homogenous and gently sloping; and (iii) sediment is not present within the SGL water column. Despite these potential weaknesses, which remain unquantified in the literature, there is presently no alternative physically-based method, and it has been applied successfully in studies for ASTER (Sneed and Hamilton, 2007) and other multispectral sensors (Georgiou et al., 2009; Morriss et al., 2013; Banwell et al., 2014; Arnold et al., 2014, Pope et al., 2016; Moussavi et al., 2016; Langley et al., 2016; Ignéczi et al., 2016), performing well both in Greenland and Antarctica.

Currently, only Morriss et al. (2013) and Ignéczi et al. (2016) have applied this method to MODIS imagery. Ignéczi et al. (2016) used it for 24–40 images over each of four melt seasons to derive maximum SGL depths for validation of their SGL depths derived from digital elevation models (DEMs). Although they used individual daily R_∞ values and calculated A_d values for each SGL, they did not present evolutions of SGL depth and volume across a series of MODIS images. Morriss et al. (2013) used the physically-based method to conclude that SGL area represents a valid proxy for volume across their study region, but individual SGL volumes or their full seasonal changes were not presented. Morriss et al.'s (2013) study was also for just one sector of the GrIS and daily R_∞ values were not calculated. Instead, a constant R_∞ value was used, meaning the Bouguer-Lambert-Beer law on which the technique relies was not calibrated for individual scenes. Finally, the g value was calibrated from relatively limited field data, whereas Pope et al. (2016) have since presented updated g values for a range of multispectral sensors, including LS8, based on extensive testing of calculated SGL water depths (derived with Eq. (2)) against *in situ* SGL spectral and bathymetric data. We therefore address our second aim by furthering the limited work above and by including Pope et al.'s (2016) developments relating to g values. Section 3.4 provides information on how we derive the parameters to be used for this physically-based approach as part of our study.

3. Approach, data and methods

3.1. Approach

Our approach comprises five methodological steps required to address the four aims of this study (identified at the end of Section 1) and therefore to achieve the overall objective of developing and applying a fully automated SGL area and volume tracking algorithm:

1. Download and pre-process MODIS and LS8 Operational Land Imager (OLI) imagery for summer 2014 (Section 3.2).
2. Evaluate three methods for generating SGL areas from MODIS imagery based on comparison with SGL boundaries derived from a supervised classification of contemporaneous LS8 images (Section 3.3).
3. Use the SGL boundaries generated by the most effective SGL area-derivation algorithm to calculate SGL depths and volumes from MODIS using a physically-based approach, and validate these measurements against LS8-derived values (Section 3.4).
4. Incorporate the best performing SGL area- and associated depth-calculation techniques into the FAST algorithm, which tracks the formation, evolution and cessation of SGLs through a sequence of satellite images during a melt season (Section 3.5).
5. Apply the FAST algorithm to the Paakitsoq and Store Glacier regions of West Greenland to investigate SGL evolution in summer 2014, including analysis of the location, timing and magnitude of rapid SGL drainage events (Section 3.6).

3.2. Satellite image collection and pre-processing

3.2.1. MODIS

Level-2 processed MOD09GQ (~250 m resolution) and MOD09GA (~500 m resolution) daily surface-reflectance datasets from 1 May to 30 September 2014 (total = 153 images) were downloaded from the USGS's LPDAAC data pool (https://lpdaac.usgs.gov/data_access/data_pool). These MODIS products are derived from data collected by the Terra satellite, which, unlike data from the Aqua satellite, have favourable illumination over the GrIS (Box and Ski, 2007). This reduces the need for discarding images that are not collected close to solar noon, which would be necessary with Aqua data. Level-2 processing helps to overcome the problem experienced by Selmes et al. (2011) where shadows within areas of complex topography in level-1 MOD02 imagery were occasionally misclassified as SGLs, meaning that an *a priori* distribution of SGLs was required to help derive SGL areas more accurately. The level-2 MOD09 data have the same position and source information as level-1 datasets, but have had an atmospheric correction algorithm (for atmospheric gases, cirrus clouds and aerosols) applied to all cloud-free pixels identified within the MOD35 cloud mask.

We used MODIS surface-reflectance data from bands 1 (red; 0.620–0.670 μm), 3 (blue; 0.459–0.479 μm) and 6 (1.628–1.652 μm). Band 4 (green; 0.545–0.565 μm) data were used to create red-green-blue (RGB) composites but were not analysed. The MODIS Reprojection

Tool Swath (version 2.2) was employed to convert raw datasets distributed as Hierarchical Data Format (HDF) files on MODIS's sinusoidal grid to common projection systems using bilinear interpolation. As part of this reprojection process, the native 231.7 m MODIS pixels were resampled to 250 m and the 463.3 m pixels were resampled to 500 m resolution, consistent with previous MODIS-based work in Greenland (e.g. Selmes et al., 2011; Liang et al., 2012; Morriss et al., 2013; Fitzpatrick et al., 2014). Only red-band data are available at near-250 m resolution, so the ratio of the red to blue band surface reflectance values from the MOD09GQ and MOD09GA products was used to sharpen data from the blue and green bands to the red band's native higher resolution (Gumley et al., 2007), a technique used previously (Box and Ski, 2007; Fitzpatrick et al., 2014). When directly comparing MODIS SGL areas, depths and volumes against those derived from LS8 imagery for evaluation and validation purposes, we used entirely cloud-free MODIS images. When analysing MODIS imagery for the whole season, a cloud filter was applied to remove pixels that had band-6 reflectance exceeding 0.15 (Box and Ski, 2007; Fitzpatrick et al., 2014). Cloud shadows were also removed by assuming that a pixel is cloud shadowed when the mean band-6 reflectance in a surrounding 21-by-21-pixel window exceeds 0.15, similar to Selmes' (2011) approach. After Liang et al. (2012), we included an additional filter to remove pixels from the analysis that were not classified as water on at least three occasions during the season, following the observation that cloud shadows have spectrally similar footprints to SGLs but are more temporally sporadic. MODIS images were cropped to the chosen study sites (Fig. 1), and ice-marginal areas were removed with the GIMP ice-sheet mask (Howat et al., 2014).

3.2.2. Landsat-8

To test and validate the SGL area- and depth-calculation methods before incorporating them into the FAST algorithm, entirely cloud-free LS8 images from 2014 were used as the training dataset: five for Paakitsoq (3 July, 11 July, 19 July, 4 August and 27 August) and six for Store Glacier (1 July, 3 July, 11 July, 2 August, 11 August and 27 August). This date range was selected to cover the key period of the melt season when SGLs are present on the GrIS. We used 30 m LS8 data from bands 2 (blue; 0.45–0.51 μm), 3 (green; 0.53–0.59 μm) and 4 (red; 0.64–0.67 μm), and 15 m data from band 8 (panchromatic; 0.50–0.68 μm), which were downloaded from the USGS Earth Explorer interface (http://earthexplorer.usgs.gov). We reprojected the images in ArcGIS to a coordinate system common with the MODIS images and cropped them to the regions of interest using the 'Extract by Mask' tool; the GIMP ice-sheet mask (Howat et al., 2014) was used to remove areas peripheral to the GrIS. Following Pope et al. (2016), atmospheric correction was not applied to the LS8 scenes. We used each image's metadata to convert digital numbers to top-of-atmosphere (TOA) reflectance and to correct for solar elevation (USGS, 2013). These TOA reflectance values represent an adequate proxy for surface reflectance (Pope et al., 2016). Table S1 presents a full list of the LS8 tiles used in our analysis.

3.3. Evaluating algorithms for deriving MODIS supraglacial lake area

We complemented Leeson et al.'s (2013) work by testing three automated methods for identifying SGL areas: (i) red/blue band thresholding (Section 2.1.1); (ii) the NDWI (Section 2.1.2); and (iii) dynamic thresholding of the red band (Section 2.1.3). We tested each method for its sensitivity to numerous threshold values, something previously unaddressed in the literature. For methods (i) and (ii), we used spatially fixed thresholds rather than adjusting them on a lake-by-lake basis or to individual study sites, since our aim was to develop a methodology that can be applied to large areas of the GrIS without any 'local' tuning. For method (iii), we chose a moving window of 25-by-25 pixels, which is the same size as Liang et al.'s (2012), but bigger than Selmes et al.'s (2011), to ensure that large SGLs were always reported. When testing these methods, we excluded all SGLs that did not reach at least two MODIS pixels (at 250 m resampled resolution) in area (i.e. 0.125 km^2) on at least one occasion in the season; we quantified the total amount of water that this procedure omits from the record by using the LS8 data for small SGLs (i.e. those <0.125 km^2). In addition, we examined the (mean and maximum) areas of the SGLs ≥ 0.125 km^2 that were excluded from the MODIS record but which were reported in the LS8 data.

Fig. 2 displays our validation methodology as a flowchart. We validated the performance of the algorithms on an image-by-image basis, as well as against a single combined dataset containing all of the LS8 images. For the LS8 images, SGL areas were calculated using a supervised classification in ArcGIS to ensure independence of the algorithm for the estimates of SGL area. We evaluated the performance of the SGL area algorithms for the MODIS imagery by comparison with the LS8-derived values for total identified SGL numbers, total identified SGL areas, the Pearson product-moment correlation coefficient of SGL areas, and the RMSE of SGL areas.

Our method of using the higher-resolution LS8 data as the validation dataset is consistent with previous studies that validated SGL areas derived from lower-resolution sensors such as MODIS against higher-resolution ones, including ASTER and Landsat, which were regarded as ground-truth data (Sundal et al., 2009; Selmes et al., 2011; Liang et al., 2012; Leeson et al., 2013; Fitzpatrick et al., 2014; Everett et al., 2016). To verify the reliability of these validation data, the SGL outlines from the ArcGIS supervised classification of the LS8 images were qualitatively compared against the SGLs present on background LS8 scenes, an approach also used to verify the validity of the training dataset in Pope et al. (2016). This indicated that the SGLs had been accurately delineated and so we could have high confidence in the validation dataset. Any false positives identified in the LS8 record by the ArcGIS supervised classification were manually removed prior to assessments of the algorithms' performance.

3.4. Deriving and validating MODIS supraglacial lake depth and volume

Once the best performing SGL area-calculation algorithm was identified (Section 3.3), we calculated SGL depths for the pixels within the SGL boundaries using Sneed and Hamilton's (2007) method (Section 2.2.2). We applied this method to MODIS's red and green bands, using Pope et al.'s (2016) updated g values for MODIS. Depths were multiplied by pixel sizes and integrated over SGL areas to provide SGL volumes. R_∞ was calculated individually for each scene from deep water in proglacial fjords. A_d was calculated image-by-image on a lake-by-lake basis by taking the mean reflectance of a ring dilated by one pixel around each SGL (Arnold et al., 2014; Banwell et al., 2014), an improvement on previous studies that used region-wide or static values (Sneed and Hamilton, 2007; Morriss et al., 2013).

LS8 depths and volumes were calculated (Eq. (2)) within the boundaries of SGLs derived from the LS8 supervised classification. To calculate them, we followed the methods of Pope (2016) and Pope et al. (2016) by averaging the SGL depths derived from LS8's red and panchromatic bands, calculated with their updated g values. We compared MODIS and LS8 pixel depths at the MODIS resolution, which required resampling of the LS8 depth arrays using a bilinear interpolation regime. This corrected for the finer resolution of LS8 imagery, which often showed deeper values towards the centre of SGLs due to LS8's smaller pixel size. By contrast, MODIS and LS8 SGL volumes were compared on a lake-by-lake basis by integrating all pixel depth values at the sensor's native resolution without any resampling. This helped to eliminate any smoothing of the results, due to resampling LS8 data to match the coarser MODIS resolution, when the calculated depths were compared on a pixel-by-basis basis. For both SGL depths and volumes, the Pearson product-

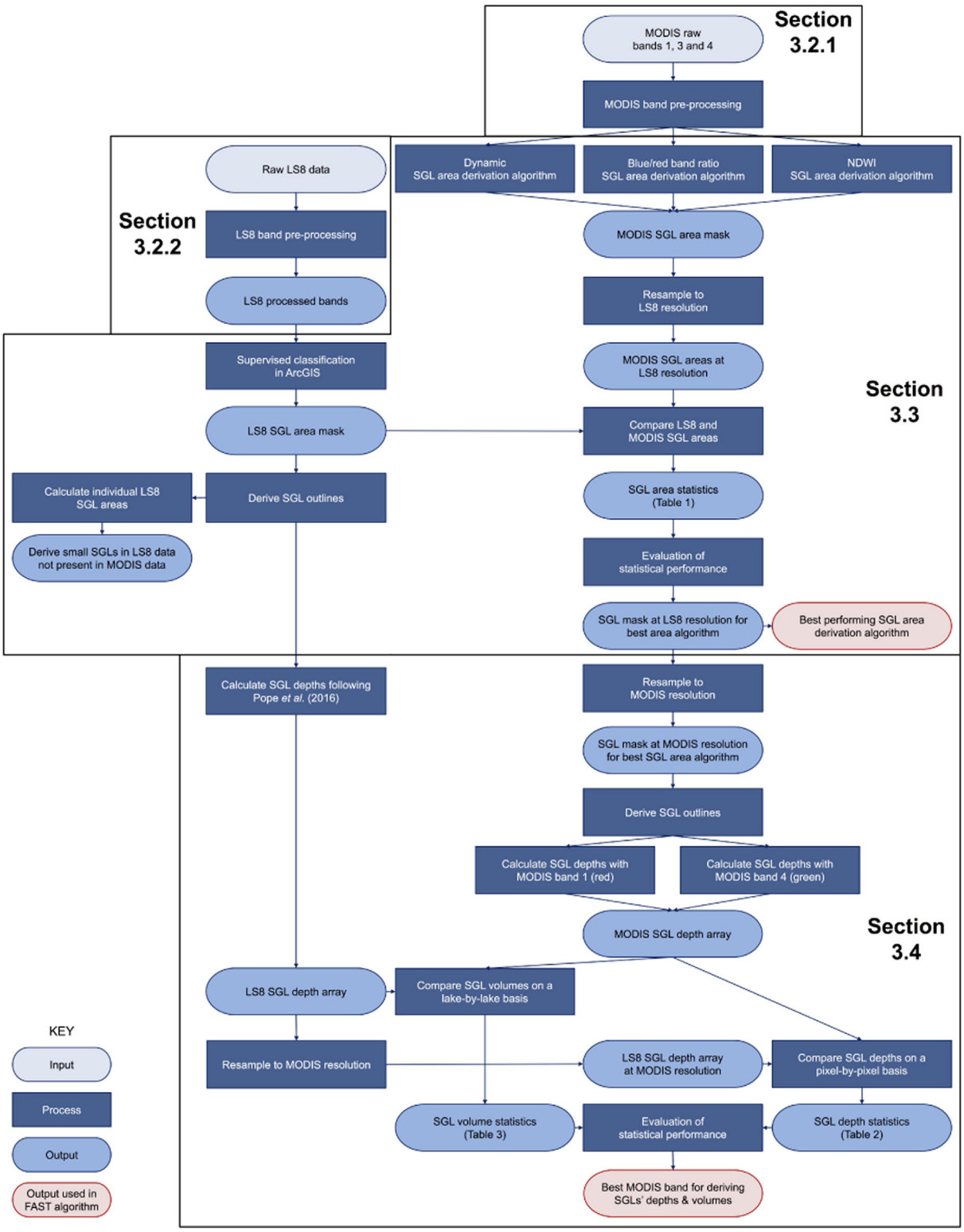

Fig. 2. Flowchart summarising the technique of validating MODIS SGL areas, depths and volumes against LS8 values. The statistical performances of the algorithms across all of the images when combined into a single dataset, as well as for each image individually, are assessed.

moment correlation coefficient and the RMSE between the two datasets were used to assess performance.

3.5. The FAST algorithm

Fig. 3 summarises the overall approach of the FAST algorithm, which was applied using the best SGL area- and depth-calculation techniques determined from the methods described in Sections 3.3 and 3.4. The only required inputs for the FAST algorithm are (i) a mask of the study region and (ii) a set of MODIS MOD09 imagery for a melt season. Both the mask and the MOD09 images must be georeferenced with the NSIDC Polar Stereographic North projection (EPSG: 3413). The algorithm can then track intra-annual changes to SGLs that reach at least two 250 m MODIS pixels

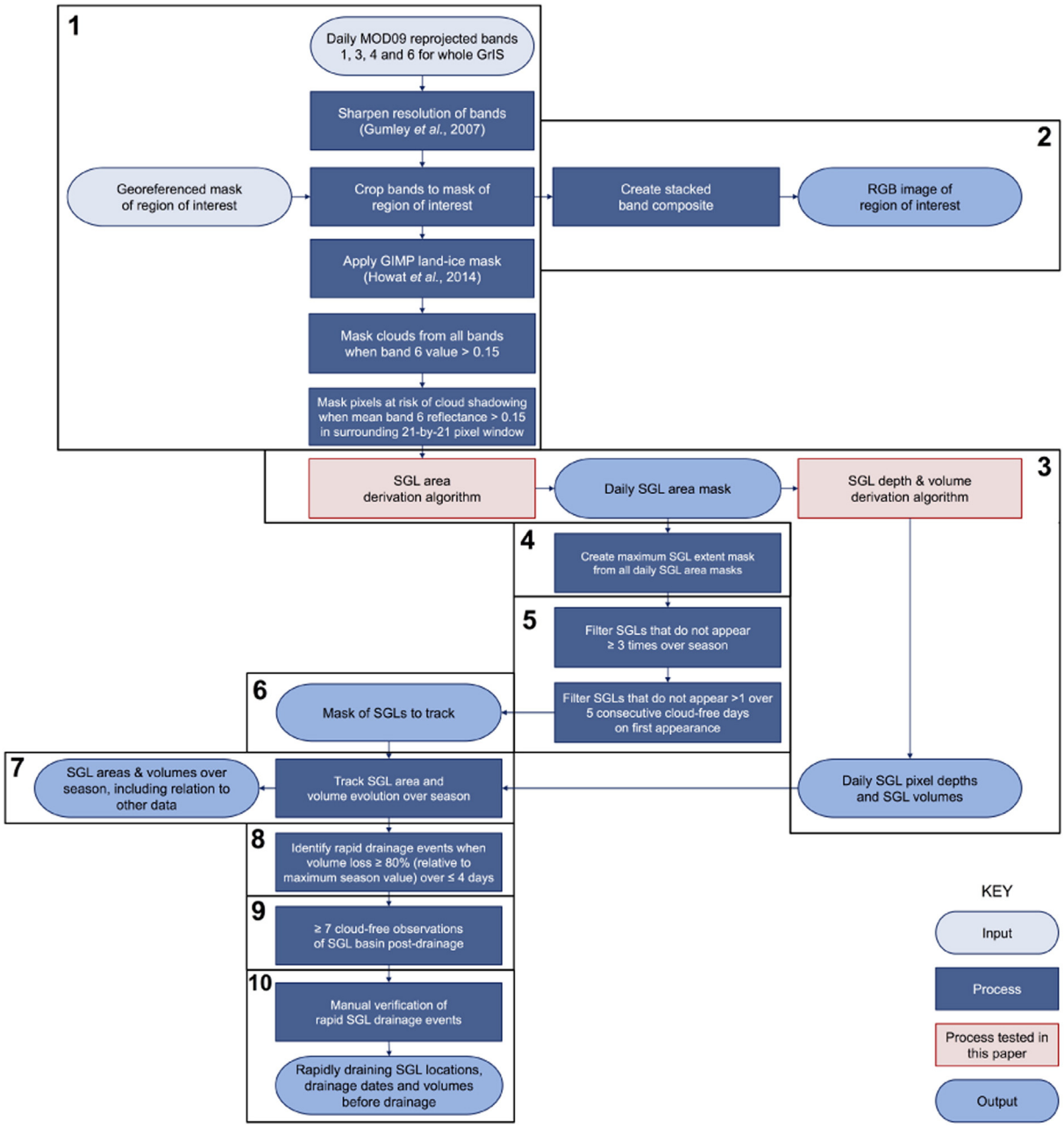

Fig. 3. Flowchart summarising the FAST algorithm, including its key inputs, processes, outputs, and the processes that are evaluated within our research. The numbers in the corners of the square black-outlined boxes refer to the steps of the FAST algorithm described in Section 3.5.

(i.e. 0.125 km^2) in area at least once in the season, and includes the following steps:

1. Pre-processing: (i) crop MODIS images to the study regions using a georeferenced mask; (ii) sharpen the resolution of MODIS's native 500 m resolution bands; (iii) mask ice-marginal areas; and (iv) remove clouds and pixels likely to be cloud shadows (see Section 3.2.1 for full pre-processing details).
2. Create stacked RGB composites of the study region.
3. Run the SGL area- and depth-calculation algorithms to derive daily SGL areas, depths and volumes.
4. Derive the maximum extents of SGLs across the season from the sum of daily SGL area masks.
5. Remove any false positive SGLs.
6. Create masks of SGLs to track across all images.
7. Track the seasonal evolution of SGL area and volume by examining, for each image in the sequence, all of the pixels within the maximum SGL extents from step (4).
8. Identify rapidly draining SGLs according to critical drainage-duration and volume-loss thresholds.
9. Remove any falsely identified rapid SGL drainage events.
10. Derive rapidly draining SGL locations, drainage dates and their water volumes prior to drainage.

In step (5), false positives are removed by filtering SGLs that do not appear at least three times over the season, and which are not observed on more than one occasion during five consecutive cloud-free observations of their basins upon their first detection (following Liang et al. (2012)). To identify rapid drainage in step (8), we assume a SGL drains by hydrofracture if it loses ≥80% of its maximum seasonal volume over a

period of ≤4 days. Although hydrofracture is generally acknowledged to occur in ≤2 days (e.g. Das et al., 2008; Tedesco et al., 2013), which is the time adopted by Selmes et al. (2011, 2013) in their studies, other workers accounted for uncertainty within satellite observations by relaxing this threshold to four days (Fitzpatrick et al., 2014; Doyle et al., 2014) or six days (Morriss et al., 2013).

Under step (9), we require there to be at least seven cloud-free observations of an empty SGL basin, with no refilling permitted, following rapid drainage; if this requirement is not met, the rapid event is removed from our analysis. To ensure that the FAST algorithm reliably identifies rapid SGL drainages within this study, all events were manually verified using the RGB composites.

For step (10), the date of SGL drainage is identified as the day on which the critical volume loss begins since this is likely to be close to the time when hydrofracture is initiated, and the ultimate focus of our research is to investigate this occurrence. Specifically, we plan to use these data in future work to investigate the relation between the initiation of hydrofracture and other local and synoptic factors that might be linked to initiating this process, possibly ultimately helping to explain the incidence of rapid SGL drainage events on the GrIS. In this study, we investigate simply the relationship between the rapidly draining SGL water volumes and the ice thicknesses beneath them, which are derived beneath SGL centroids from the GrIS terrain data of Morlighem et al. (2014).

3.6. Study sites

The two study sites (Fig. 1) were used to evaluate the three SGL area-derivation algorithms (Section 3.3), to validate the SGL depth-derivation technique (Section 3.4), and to generate the first output dataset from the FAST algorithm (Section 3.5). We chose these two regions as they allow the suitability of the methods to be investigated in both terrestrial and marine-terminating sectors of the GrIS; moreover, both areas are the foci of previous and ongoing research on supraglacial and subglacial hydrology, and ice-sheet dynamics (e.g. Catania et al., 2008; Colgan et al., 2011b; Banwell et al., 2012, 2013, 2014, 2016; Arnold et al., 2014; Todd and Christoffersen, 2014; Ryan et al., 2015; Fried et al., 2015).

4. Results

4.1. Supraglacial lake area

4.1.1. Performance of supraglacial lake area-calculation algorithms

Initially, the two study regions are considered independently to determine which area-delineation method and threshold is best for each; the data are then combined into a single dataset for both regions to elicit the best performing threshold across both of them. Table 1 presents the results for SGL areas for the MODIS images that overlap (temporally and spatially) with the LS8 images, calculated with the three best performing thresholds for each area-derivation technique. Fig. 4 shows a comparison of SGL areas calculated for the best threshold value with each algorithm at each site. Some false positives were identified by the area-derivation algorithms — for example, see the black box on Fig. 5(a). Dynamic thresholding of the red band generally outperforms the other approaches for both regions in terms of RMSEs and the percentage of SGLs reported by MODIS relative to the total number of SGLs reported in the LS8 dataset (Table 1). While the other methods with specific thresholds occasionally result in higher r values, they are less accurate than the dynamic red band thresholding method in terms of RMSEs and reported percentages of SGLs (Table 1). Although less accurate than the dynamic red band thresholding method, the NDWI and blue/red band ratio thresholding methods perform better at Paakitsoq than Store Glacier: RMSEs for the NDWI and blue/red band ratio thresholding approaches are <0.40 km^2 at Paakitsoq but >0.40 km^2 at Store Glacier. Our results show that dynamic thresholding is the only approach that can be applied with similar threshold values across different regions of the GrIS. The best performing values for dynamic thresholding are nearly identical between Paakitsoq and Store Glacier, with the threshold value of 0.640 at Store Glacier only marginally outperforming the 0.645 value for Paakitsoq in terms of number of SGLs reported (Table 1). This compares with the best performing threshold values for the NDWI (or blue/red band thresholding) approach, which were 0.125 (or 0.775) in the Paakitsoq region and 0.190 (or 0.710) at Store Glacier. The red/blue band thresholding performs significantly less accurately at Store Glacier, with higher RMSEs, lower r values and lower SGL numbers reported. Even though a threshold value of 0.710 performs best, with a RMSE of 0.418 km^2 — similar to the RMSEs for the other algorithms — use of this threshold value results in an exceptionally low reporting of SGL numbers (only 10.1%) compared with the LS8-derived SGLs.

Table 1
Performance indicators for the best performing SGL area-calculation algorithms tested at the study sites. All r values are significant at the 95% confidence interval (p-value < 0.05). The best performing algorithm and threshold at each site is highlighted in bold italicised text. Full results for all thresholds tested are presented in Table S1.

Region	SGL area algorithm	Threshold value	Total LS8 SGL area (km^2)	LS8 SGL number	Total MODIS SGL area (km^2)	Difference (%) in SGL area	Number of LS8 SGLs predicted	Detection (%) of LS8 SGLs	RMSE (km^2)	r
Paakitsoq	***Dynamic***	0.640	173.7	406	110.1	36.6	161	39.7	0.338	0.706
		0.645			***114.3***	***34.2***	***169***	***41.6***	***0.338***	***0.702***
		0.650			117.6	32.3	171	42.1	0.341	0.696
	NDWI	0.120			94.7	45.5	106	26.1	0.368	0.752
		0.125			82.2	52.7	95	23.4	0.369	0.762
		0.130			73.8	57.5	86	21.2	0.374	0.760
	Blue/red band ratio	0.770			74.1	57.3	87	21.4	0.374	0.760
		0.775			79.2	54.4	90	22.2	0.371	0.760
		0.780			84.4	51.4	96	23.6	0.372	0.755
Store Glacier	***Dynamic***	0.635	121.3	298	77.2	36.4	133	44.6	0.301	0.679
		0.640			***79.1***	***34.7***	***135***	***45.3***	***0.301***	***0.678***
		0.645			81.2	33.0	135	45.3	0.303	0.674
	NDWI	0.180			21.2	82.5	34	11.4	0.425	0.487
		0.190			17.2	85.8	30	10.1	0.418	0.541
		0.195			15.3	87.4	29	9.7	0.419	0.563
	Blue/red band ratio	0.710			27.3	77.5	40	13.4	0.458	0.417
		0.750			54.8	54.8	55	18.5	0.871	0.199
		0.760			63.9	47.3	63	21.1	0.942	0.196

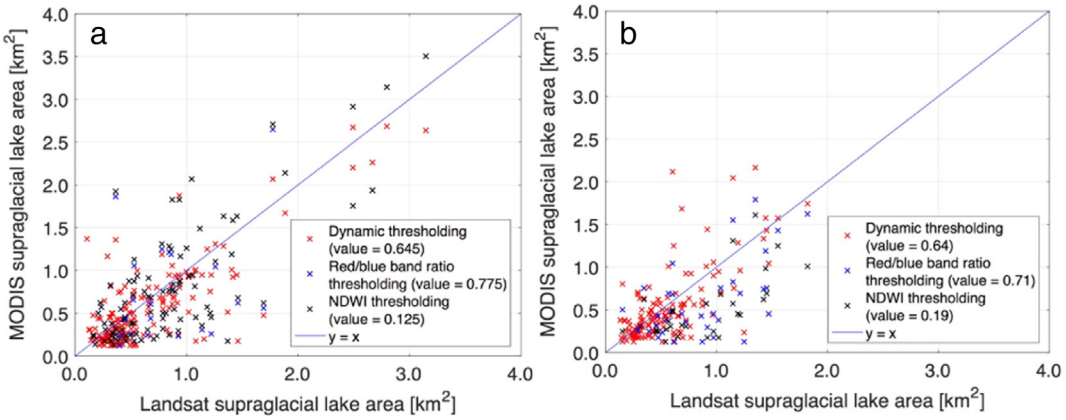

Fig. 4. SGL areas derived from the algorithms applied to MODIS imagery compared with SGL areas derived from the LS8 supervised classification for the (a) Paakitsoq and (b) Store Glacier regions. Data shown are for the best performing threshold value for each SGL area-delineation technique. The blue lines on both subplots show $y = x$. Note that only SGLs predicted by both the MODIS area-derivation technique and the LS8 supervised classification are plotted.

It is more helpful to have a single uniform threshold value across both regions to allow it to be incorporated into a fully automated approach. Therefore, SGL areas derived from MODIS with threshold values in the range 0.640 to 0.645 (i.e. the best performing thresholds for the two regions) at 0.001 increments are compared with LS8 SGL areas. This determines that the 0.640 threshold is best, for which we obtain a final RMSE value for SGL area calculations of 0.323 km^2, an r of 0.694, and a total of 42% of the LS8 SGLs reported (Fig. 6). Thresholds between 0.641 and 0.645 perform marginally worse ($r = 0.690$–0.693, with all p-values < 0.01; RMSE = 0.324 km^2; reported LS8 SGL number remains at 42%). We find no obvious spatial pattern in terms of SGLs that are reported in the LS8 dataset but which are absent from the MODIS record: SGLs at all elevation bands and within regions of both dark and bright surrounding ice are reported equally well, but, similarly to Leeson et al. (2013), we see that the areas of SGLs with partial ice cover are under-estimated (e.g. see outlines on Fig. 5).

4.1.2. Supraglacial lakes omitted from the MODIS record

To quantify the impact of using the coarser-resolution MODIS product on the reporting of total SGL areas, we assess the areas classified as water-covered from the LS8 supervised classifications that are less than two MODIS pixels in size. It is important to note that the values presented here represent all water-covered areas identified from the LS8 supervised classification, so while these numbers will involve some smaller SGLs, water contained within supraglacial streams and slush zones, for example, will also be included. Across the LS8 imagery, areas of contiguous water covering <0.125 km^2 in area represent an average total per image of 3.84 km^2 (range 0.29–9.61 km^2) for Paakitsoq and 1.99 km^2 (range 0.11–4.86 km^2) for Store Glacier. These compare with the much higher average regional cover by SGLs ≥ 0.125 km^2 recorded in the MODIS images of 22.02 km^2 (Paakitsoq) and 13.18 km^2 (Store Glacier). Relative to the sizes of the ice-covered regions, these values for area covered by SGLs < 0.125 km^2 in size represent coverages of only 0.077% (Paakitsoq) and 0.037% (Store Glacier). Compared with the areas covered by SGLs in the MODIS imagery, these other water-covered areas represent only 17.4% (Paakitsoq) and 15.1% (Store Glacier) of the total water-covered areas identified by MODIS. These small SGLs have a mean size of 0.006 km^2 at both Paakitsoq and Store Glacier.

In addition to the small (<0.125 km^2) SGLs that could never be identified in MODIS imagery due to its coarse resolution, we examine the size distribution of SGLs ≥ 0.125 km^2 (and so which could theoretically be identified by MODIS) that are present in the LS8 record but which are not identified in the MODIS SGL classification scheme (using a dynamic band threshold value of 0.640). At Paakitsoq, the SGLs omitted

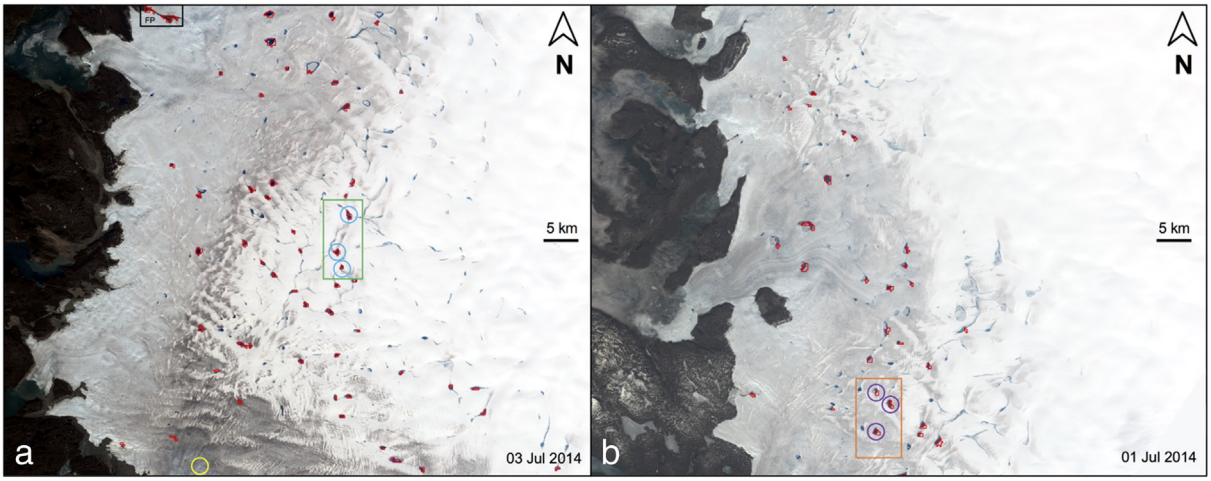

Fig. 5. SGL perimeters, shown in red, as derived using a dynamic thresholding approach applied to MODIS's red band with a threshold value of 0.640 for both the (a) Paakitsoq and (b) Store Glacier regions, overlain onto background LS8 images (see Table S1 for image details). The total areal extents within panels (a) and (b) are equivalent to those shown in Fig. 1(a) and (b). A false positive SGL is highlighted in (a) within the black box labelled 'FP'. The blue circles in (a) and purple circles in (b) indicate SGLs that drain rapidly as part of a cluster (Section 5.3.1). The areas within the green box on (a) and orange box on (b) indicate the areas contained within the subplots of Fig. 14. The yellow circle in (a) indicates the area within which a SGL drains, refills and then re-drains (Section 5.3.1), although the SGL is absent from this image.

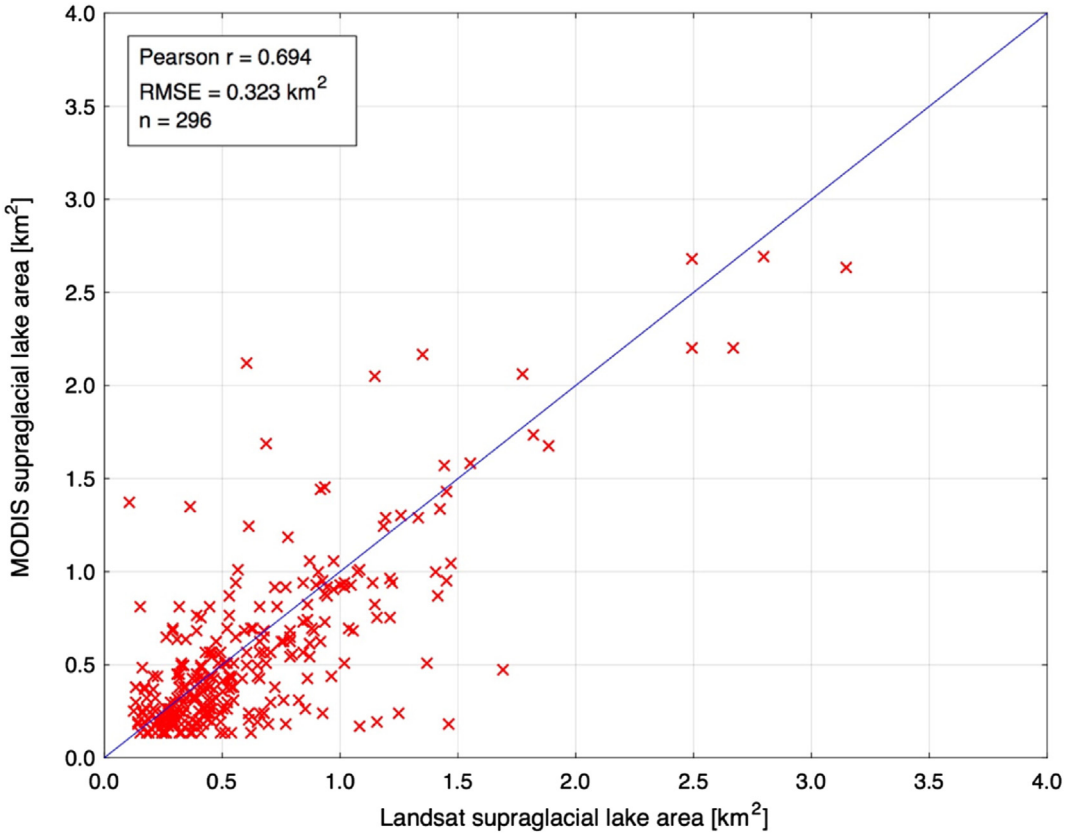

Fig. 6. SGL areas across both study sites derived from MODIS imagery using a dynamic thresholding approach applied to the red band with a threshold value of 0.640 compared with SGL areas ascertained from the LS8 supervised classification. *n* represents the number of data points on the graph. The blue line shows $y = x$. The *r* value is significant with a p-value of <0.01.

from the MODIS record have a mean area of 0.26 km^2 (maximum 1.20 km^2) and at Store Glacier, these SGLs have a mean area of 0.27 km^2 (maximum 1.08 km^2). These are relative to mean SGL areas within the MODIS-reported SGL populations of 0.69 km^2 (Paakitsoq) and 0.59 km^2 (Store Glacier). An unpaired Student's *t*-test reveals a statistically significant difference between the SGL areas for the populations of SGLs reported by LS8 that are absent from the MODIS record and the SGLs that are reported by both MODIS and LS8: for Paakitsoq, $t = 8.4$, with a p-value of <0.01; for Store Glacier, $t = 6.4$, with a p-value of <0.01. Overall, this analysis indicates that smaller SGLs tend to be omitted from MODIS data while being reported in LS8 data.

4.2. Supraglacial lake depths and volumes

4.2.1. Performance of the supraglacial lake depth-calculation algorithm

Tables 2 and 3 present results from the MODIS-based calculations of SGL depth and volume with the green and red bands, compared with the corresponding LS8-based depths and volumes, which were calculated using LS8's red and panchromatic bands as inputs to the physically-based approach. Depths and volumes calculated with MODIS's red band significantly outperform those from the green band for both sites. For the red band, RMSEs for SGL pixel depths are 1.19 m (Paakitsoq) and 1.39 m (Store Glacier), relative to a mean MODIS pixel depth for water-covered pixels of 1.40 m across SGLs from all of the images. RMSEs for SGL volumes are 6.1×10^7 m^3 (Paakitsoq) and 5.7×10^7 m^3 (Store Glacier), relative to a mean MODIS SGL volume of 4.0×10^7 m^3 for SGLs from all of the images. Green band RMSEs are always more than double these values. In general, the MODIS-derived SGL depths and volumes are lower than the LS8 ones, particularly for depths < ~4 m, although there is spread in the data (Figs. 7 and 8). There are two dates for which this pattern does not obviously apply. The first is

Table 2
Summary of the performance of MODIS SGL depths derived from the red and green bands compared with LS8 depths derived from the average of the red and panchromatic bands across both study sites for each image date. All values of *r* except the one marked with an asterisk are significant at the 95% confidence interval (p-value < 0.05). Summary data for the best performing band (i.e. band 1, red) across all days are shown in bold italicised text.

Region	MODIS band tested	Date (2014)	*n*	*r*	RMSE (m)
Paakitsoq	Band 1 (red)	03 Jul	213	0.675	1.11
		11 Jul	157	0.134*	1.45
		19 Jul	215	0.610	1.08
		04 Aug	225	0.668	1.29
		27 Aug	152	0.649	0.95
		All	***962***	***0.447***	***1.19***
Store Glacier	Band 1 (red)	01 Jul	121	0.427	1.88
		03 Jul	137	0.388	1.49
		11 Jul	161	0.221	0.94
		02 Aug	101	0.419	1.35
		11 Aug	111	0.575	1.30
		27 Aug	72	0.497	1.21
		All	***703***	***0.259***	***1.39***
Paakitsoq	Band 4 (green)	03 Jul	212	0.659	6.30
		11 Jul	158	0.160	10.22
		19 Jul	214	0.570	6.89
		04 Aug	107	0.329	3.33
		27 Aug	151	0.668	6.48
		All	842	0.298	7.11
Store Glacier	Band 4 (green)	01 Jul	121	0.381	4.96
		03 Jul	137	0.385	5.86
		11 Jul	161	0.176	7.52
		02 Aug	102	0.380	10.54
		11 Aug	111	0.542	11.64
		27 Aug	71	0.425	11.10
		All	703	0.233	8.59

Table 3
Summary of the performance of MODIS SGL volumes derived from the red and green bands compared with LS8 values derived from the average of the red and panchromatic bands across both study sites for each image date. All values of r are significant at the 95% confidence interval (p-value < 0.05). Summary data for the best performing band (i.e. band 1, red) across all days are shown in bold italicised text.

Region	MODIS band tested	Date (2014)	n	r	RMSE (km^3)
Paakitsoq	Band 1 (red)	03 Jul	48	0.881	0.050
		11 Jul	50	0.456	0.045
		19 Jul	23	0.897	0.088
		04 Aug	25	0.974	0.066
		27 Aug	13	0.963	0.085
		All	***159***	***0.777***	***0.061***
Store Glacier	Band 1 (red)	01 Jul	27	0.803	0.082
		03 Jul	27	0.741	0.065
		11 Jul	30	0.446	0.040
		02 Aug	16	0.897	0.049
		11 Aug	18	0.958	0.023
		27 Aug	11	0.918	0.045
		All	***129***	***0.673***	***0.057***
Paakitsoq	Band 4 (green)	03 Jul	47	0.813	0.123
		11 Jul	50	0.693	0.353
		19 Jul	22	0.558	0.220
		04 Aug	25	0.967	0.570
		27 Aug	12	0.966	0.390
		All	156	0.795	0.339
Store Glacier	Band 4 (green)	01 Jul	27	0.810	0.072
		03 Jul	27	0.743	0.127
		11 Jul	30	0.559	0.263
		02 Aug	16	0.826	0.455
		11 Aug	18	0.940	0.413
		27 Aug	11	0.928	0.297
		All	129	0.674	0.279

11 July at Paakitsoq, shown on Figs. 7(a) and 8(a), where SGL pixel depths and volumes tend to be higher in the MODIS than the LS8 images. Further investigation shows that the 11 July LS8 image includes regions, which are mainly on the ice sheet, that are covered by a light white banding, interpreted to be very fine high-level clouds, aerosol or dust, which could explain the seemingly low LS8 pixel depths calculated for this image. The second major anomaly is the sharp positive tail for the SGL depths and volumes at Paakitsoq on 4 August (Fig. 7(a)). This may result from the difficulty in accurately resolving water depths > ~4 m when using LS8's red and panchromatic bands for the physically-based method (Moussavi et al., 2016). This, therefore, likely indicates a limitation with the validation dataset rather than with the approach as applied to the MODIS data. In Fig. 8(a), SGL volumes are, however, not similarly overestimated for MODIS SGLs compared with LS8 ones, which suggests that resampling the LS8 depth arrays to match the MODIS resolution offsets this bias to a degree. For all of the images, there is no tendency for higher SGL depth errors to be present for specific elevation bands or for given SGL sizes (Figs. 7, 8 and 9).

When the differences between MODIS and LS8 depths are averaged across all of the images, the mean differences are small, with the vast majority of SGLs displaying errors in the range –0.5 to 0.5 m (Fig. 9). Errors of ~ −3 m (i.e. red values on Fig. 9), where MODIS depths are higher than LS8 ones, are possibly due the effect described above, where MODIS records deeper water than LS8 due to the limited sensitivity of the LS8 method at higher depths. Errors of ~ +3 m (i.e. blue values on Fig. 9), where LS8 values are consistently higher than MODIS ones, may be the competing effect, which results from the coarse resolution of MODIS, meaning that, on some days, the deepest water pixels within SGLs were not recorded accurately within the MODIS surface-reflectance data, and were instead sampled as lighter (and so shallower) water pixels. This possible bias towards the sampling of brighter pixels in MODIS may also result in the derivation of higher A_d values in MODIS than in LS8, which would lead to the reporting of lower SGL depths by MODIS than LS8. Combining the red band MODIS-derived SGL pixel depths and volumes to form single samples across both study regions, the final RMSE values are 1.27 m for SGL depth and 5.9×10^7 m^3 for SGL volume (Fig. 10). Although both values are statistically significant (p-value < 0.01), r is greater for SGL volumes ($r = 0.741$) than depths ($r = 0.365$), likely due to the fewer data points and lower spread within the SGL volume dataset. These calculated errors are applied to the SGL depths and volumes calculated by our FAST algorithm for MODIS imagery. These combined data display a similar pattern to the region-specific data, with a tendency for MODIS values to be underestimated compared with LS8 ones, but with some scatter. This pattern also broadly matches that observed for the LS8 versus MODIS SGL area comparisons (Fig. 6).

We investigate whether there is bias in the errors for the data for lower (or higher) SGL depths and volumes. MODIS depth measurement errors show little variation (mean = 1.16 m; σ = 0.12 m; range = 1.00–1.24 m) for water ≤ 4 m deep, but they are almost three times higher (RMSE = 2.99 m) for water > 4 m deep (Table 4). A similar pattern exists for SGL volumes (Table 5), where SGLs with volumes $<1.0 \times 10^8$ m^3 have lower errors for and variation within their measurements (mean = 5.6×10^7 m^3; σ = 1.2×10^7 m^3; range = $3.9–8.0 \times 10^7$ m^3) than SGLs exceeding this volume (RMSE = 1.1×10^8 m^3). This pattern of errors may be partially explained by this study's use of the longer-wavelength red and panchromatic bands from LS8 data to derive the SGL depths and volumes within the validation dataset. These longer wavelengths attenuate more quickly within the water column than shorter wavelengths, such as LS8's green band, and this may result

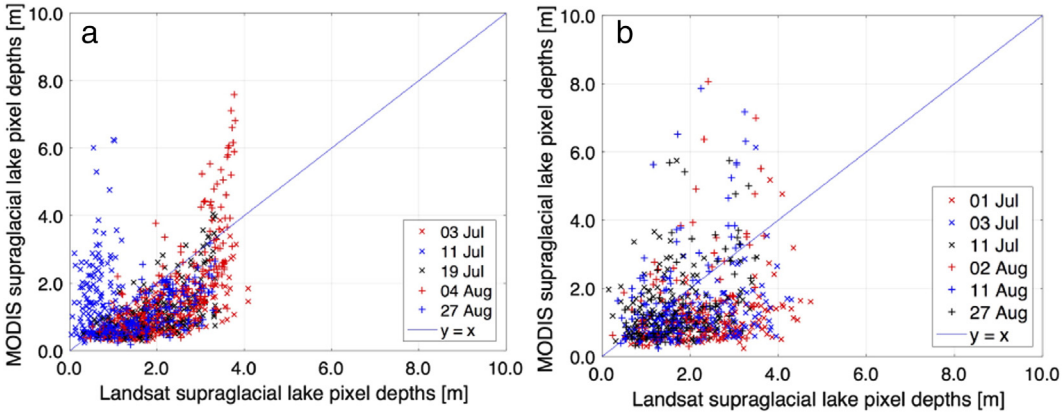

Fig. 7. SGL pixel depths calculated from MODIS's red band for the (a) Paakitsoq and (b) Store Glacier regions, compared with those calculated from the average of LS8's red and panchromatic bands. The blue lines on both subplots show $y = x$. Note the two anomalous sets of SGL pixel depths for Paakitsoq on 11 July and 4 August, where the MODIS values are systematically higher than the LS8 values.

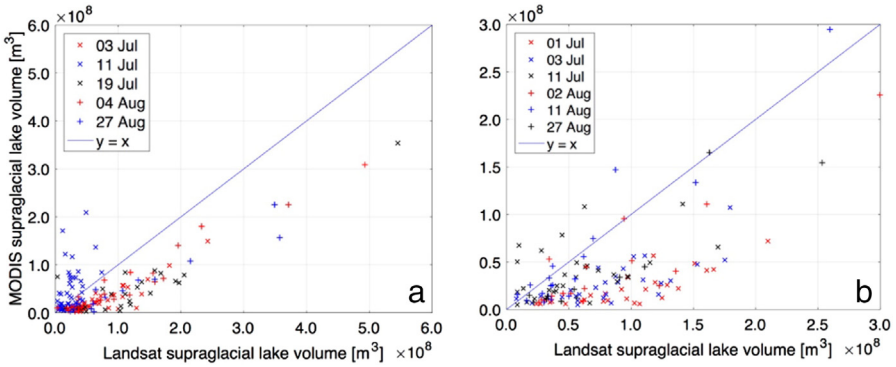

Fig. 8. SGL volumes (calculated by integrating the SGL pixel depths) derived from MODIS's red band for the (a) Paakitsoq and (b) Store Glacier regions, compared with those calculated from the average of LS8's red and panchromatic bands. The blue lines on both subplots show $y = x$. Note the anomalous set of SGL volumes for Paakitsoq on 11 July, where the MODIS values are systematically higher than the LS8 values.

in the LS8 data's bias against the deepest (>4 m) water (Moussavi et al., 2016).

4.2.2. Supraglacial lake volume scaling

Using the single sample of SGL volumes for both regions, a regression of MODIS-derived SGL volumes against LS8-derived SGL volumes yields a slope coefficient of 0.721 (Fig. 10(b)). Scaling the MODIS SGL volumes accordingly (i.e. by dividing them by the slope coefficient of 0.721), and comparing them with the LS8 values, reduces the RMSE slightly from 5.9×10^7 m^3 to 5.4×10^7 m^3. Depth-based scaling is not attempted because, when the depths were compared, this was done on a pixel-by-pixel basis; whereas for the volumes, comparisons were conducted on a lake-by-lake basis, for which no resampling was required.

4.3. Supraglacial lake evolution at Paakitsoq and Store Glacier

When applied to the study sites in summer 2014, the FAST algorithm tracks individual area and volume changes for 202 SGLs at Paakitsoq and 122 SGLs at Store Glacier, the first time that an automatic derivation of seasonal changes to SGL volume has been possible on the GrIS. For each day of the analysis, individual SGL areas and volumes are integrated to obtain the total SGL areas and volumes across the regions. Broadly similar patterns are observed for both sites, with gradual increases in SGL area and volume in the early melt season, peaks in total stored SGL water in mid-July and early August, and then decreasing SGL area and water volume from mid-August onwards (Fig. 11). For both regions, there is a statistically significant correlation (with high r values) between the total number of SGLs on an image and the total volume of water contained within SGLs for that image (Fig. 12). However, there is no statistically significant relationship between the total number of SGLs on an image and the mean SGL volume for the SGLs on that image, although the relationship is stronger at Store Glacier ($r = 0.469$) than Paakitsoq ($r = -0.008$) (Fig. 12).

Table 6 summarises results from the identification of rapid SGL drainage events using the FAST algorithm, with full drainage-event details in Tables S4 and S5. The mean surface elevation at which rapid SGL drainage events occur is ~1050 m in both regions, and both regions also exhibit similar median dates of rapid drainage initiation: 12 July (Paakitsoq) and 7 July (Store Glacier). However, the modal dates of rapid drainage vary more between the two regions: 13 July (Paakitsoq) and 3 July (Store Glacier). There is an obvious upglacier, seasonal progression of rapid SGL drainage in both regions, and 37% of rapid events occur from 9 to 18 July (Fig. 13). The fewer late-season (i.e. post-18 July) rapid drainage events may result from increasing regional cloud cover during this later period (cf. Fig. 11), meaning that rapid SGL drainage could not be identified with certainty.

5. Discussion

5.1. Performance of the supraglacial lake area-calculation algorithms

The first aim of this study was to evaluate a variety of methods that are commonly used to automatically classify SGL areas from MODIS imagery since a consensus on the best method to use has not yet emerged. In doing this, our study complements Leeson et al.'s (2013) testing of numerous SGL area-derivation methods, but builds on that work by also testing a range of threshold values for the different methods. We found that a dynamic thresholding technique applied to MODIS's red band with a threshold value of 0.640 performs best among the algorithms tested. The RMSE of 0.32 km^2 for this method is higher than values reported in some other studies (e.g. 0.14 km^2 in Fitzpatrick et al. (2014); 0.20 km^2 in Liang et al. (2012); 0.11 km^2 in Selmes et al. (2011); 0.22 km^2 in Sundal et al. (2009); 0.08 km^2 in Everett et al. (2016)), but is lower than Leeson et al.'s (2013) value of 0.48 km^2 for dynamic thresholding of the red band. However, these studies used a range of validation data derived from different techniques for different regions and areal extents of the GrIS, which likely explains the differences in performance compared with this study. For example, the MODIS SGL areas in our work were compared against LS8 SGL areas from a supervised classification, while previous research validated them against manually derived SGLs (e.g. Leeson et al., 2013; Everett et al., 2016) or other validation data. In addition, our higher RMSE may be because the earlier studies only compared specific-sized SGLs or subsets of a complete population: for example, Liang et al. (2012) included only 63 SGLs in their sample rather than the complete dataset used here. Our use of the entire SGL population allows for more robust comparisons than if a subset of SGLs had been used. We identified a similar percentage of the total number of SGLs present within the validation dataset as other studies (e.g. Leeson et al., 2013). Using dynamic thresholding of the red band without an *a priori* distribution of SGLs appears to have had only a minor impact on the overall percentage of SGL numbers reported compared with Leeson et al.'s (2013) value. However, it is feasible that omitting this pre-defined distribution leads to the lower accuracy (in terms of the RMSE) of SGL areas compared with SGL areas in other studies (Selmes et al., 2011; Everett et al., 2016).

Dynamic thresholding of the red band is sensitive to the chosen threshold value, with values of 0.635–0.650 performing the best depending upon the region investigated (Table 1). Using this method, the marginally higher performance (based upon the RMSE and r values) for a threshold of 0.645 for the Paakitsoq region can likely be attributed to the large areas of dark ice, and so low albedo, present within this region compared with Store Glacier (see the differing ice darkness on Figs. 5(a) and (b)). We investigate whether this difference in background albedo is meaningful by comparing surface-reflectance values for all visible spectral bands across all of the ice-covered areas of our

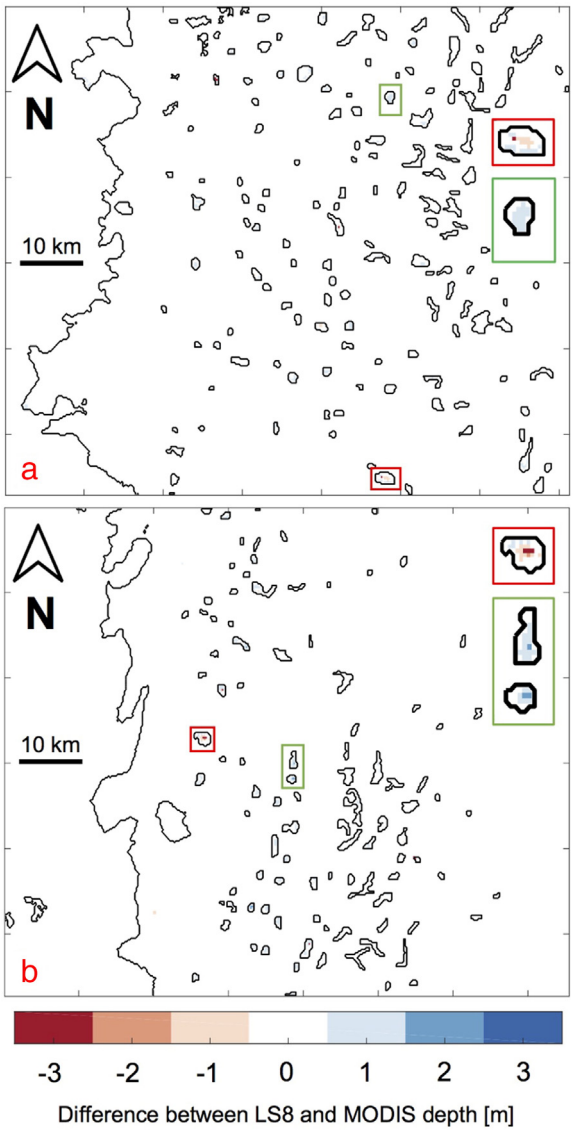

Fig. 9. The mean difference (derived by averaging the difference between pixel water depths across all images) between SGL depths for the (a) Paakitsoq and (b) Store Glacier regions, highlighting the lack of spatial or elevation bias in the errors of SGL water depth. A positive difference indicates that the MODIS SGL depth has been underestimated compared with the LS8 depth, and vice versa. To allow these comparisons, the LS8 depths were resampled using a bilinear technique to 250 m resolution and the MODIS depths were retained at their native 250 m resolution. The GrIS margin is shown by the thick black line on both subplots, and the areas within the plots are equivalent to those shown within Fig. 1. The SGL boundaries shown are derived from the sum of the SGL extents across all of the LS8 images. The green insets on both subplots are higher-scale examples of the observation of consistently higher LS8 depths towards SGL centres compared with MODIS values. The red insets on both subplots are higher-scale examples of where MODIS predicts deeper water than LS8 over SGL centres, possibly due to the limited sensitivity of the LS8 method at very high depths.

two regions. To ensure similar illumination, this is conducted for the LS8 tiles that were obtained from the same pass of the LS8 satellite across both study regions (i.e. for the passes on 3 July, 11 July and 27 August; Table S1). Since albedo measures diffuse reflection and here we are comparing surface-reflectance values (i.e. directional-hemispherical reflection), we note that these values represent only a first-order approximation. We find a mean directional-hemispherical reflection for all bands of 0.64 ($\sigma = 0.078$) for Paakitsoq and 0.67 ($\sigma = 0.097$) for Store Glacier, with a similar pattern for the red band: directional-hemispherical reflection of 0.61 ($\sigma = 0.072$) for Paakitsoq and 0.66 ($\sigma = 0.092$) for Store Glacier. With the darker background ice at Paakitsoq, the mean overall reflectance in the moving window used for dynamic thresholding is lower than at Store Glacier, and so a slightly higher threshold is needed to define a SGL at Store Glacier than at Paakitsoq. Even with this effect represented at these sites, the performance of the dynamic thresholding technique was not markedly affected by differing thresholds and at Paakitsoq a value of 0.640 performed nearly as well as the threshold value of 0.645. Overall, this indicates that there is a broad peak in performance for threshold values in the 0.635–0.650 range across the GrIS, also justifying Selmes et al.'s (2011) use of a 0.650 threshold.

Although the NDWI and blue/red band thresholding approaches perform relatively poorly compared to the dynamic thresholding method, once the thresholds for these methods were tuned for the specific study regions, their RMSEs for SGL area (Table 1) were lower than those for some other SGL area algorithms examined by Leeson et al. (2013): they found RMSEs of 0.78 km^2 (using Sundal et al.'s (2009) method) and 0.95 km^2 (using Johansson and Brown's (2013) method) when comparing automatic versus manually derived MODIS SGLs. Thus, applying the blue/red band thresholding and NDWI approaches to specific regions of the GrIS can be defended, but only with adjustment of thresholds either on a site-by-site basis (Fitzpatrick et al., 2014) or even on a lake-by-lake basis (Box and Ski, 2007). However, this would be problematic for applying thresholds across larger areas of the GrIS and for their incorporation into automated methodologies of SGL detection and tracking, such as that developed in our study. Lower performance for the NDWI and blue/red band thresholding methods compared to dynamic thresholding of the red band may also result from the sharpening of MODIS's 500 m native resolution blue band to match that of the 250 m red band, meaning blue-band values are smoothed and the ratio between the highly-attenuating red and the lower-attenuating blue bands becomes diminished (Selmes, 2011).

5.1.1. Supraglacial lakes omitted from MODIS imagery

As part of our study's first aim, it was necessary to quantify the impact of using MODIS imagery on the reporting of total SGLs on the GrIS, particularly to determine whether the use of coarser-resolution imagery represents a sufficient trade-off in terms of its spatial resolution to exploit its higher temporal resolution. Our work indicates that using coarse-resolution MODIS imagery results in the omission of numerous SGLs in two main ways. The first category of SGLs omitted from the MODIS record are those <0.125 km^2 (as measured by LS8) and therefore which could never be resolved within the MODIS record because they are below MODIS's threshold reporting area. Our results show that these small SGLs represent only a small percentage relative to the regional coverage by SGLs ≥ 0.125 km^2 and which are identified by MODIS. Although these values are low, use of MODIS imagery alone potentially misses SGLs within this category that may be capable of hydrofracture: Krawczynski et al. (2009) indicate SGLs ≥ 0.25 km in diameter (i.e. with areas ≥ 0.0491 km^2 when approximated as perfect circles) can fracture through subfreezing ice 1 km thick in low-tension regions of the GrIS. We investigate the data to determine the number of SGLs in the study regions that meet this criterion (i.e. with sizes of 0.0491–0.125 km^2) by creating a maximum SGL extent mask from the LS8 images. We find 189 SGLs that grow to within this size range but do not grow beyond it at least once in the season in the Paakitsoq region, and 89 in the Store Glacier region. The second category of SGLs omitted from the MODIS record are those that are theoretically large enough to be identified by MODIS (i.e. ≥0.125km^2), but which are not identified as part of the SGL area-classification scheme. The SGL area-derivation algorithm used in this study resulted in the reporting of only 42% of all of the LS8 SGLs ≥ 0.125 km^2 in area. By investigating the area of the SGLs ≥ 0.125 km^2 reported by LS8 but not by MODIS, we showed that these unreported SGLs tended to be smaller than the mean size of the MODIS-reported SGLs within both regions (Section 4.1.2). This indicates that MODIS can more reliably identify larger SGLs than those that lie closer

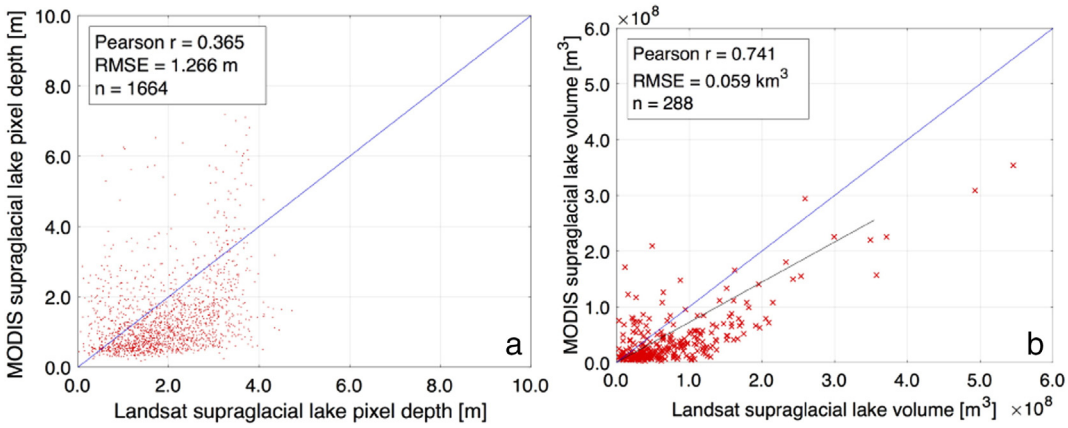

Fig. 10. SGL (a) pixel depths and (b) volumes across both study sites derived using MODIS's red band compared with depths and volumes derived from LS8's red and panchromatic bands. The blue lines on both subplots show $y = x$. The black line on (b) is an ordinary least-squares linear regression, $y = 0.721(x)$, which forms the basis of the SGL volume scaling relationship described in Section 4.2.2.

to its threshold reporting area of 0.125 km^2. This under-reporting by MODIS replicates Leeson et al.'s (2013) findings.

Overall, these results suggest that using the MODIS record in isolation from spatially finer records is unlikely to introduce significant loss of information on the hydrology of the GrIS since a high percentage of SGLs is included in the MODIS record. To be able to capture the drainage of these small SGLs, which may be capable of hydrofracture (Krawczynski et al., 2009), a dataset with the spatial resolution of (at least) the LS8 sensor but with MODIS's near-daily temporal resolution is required. A combined record of LS8 and Sentinel-1 SGL observations holds promise in this regard (Miles et al., in review).

5.2. Performance of the supraglacial lake depth-calculation algorithm

The study's second aim was to apply a physically-based depth-calculation algorithm to the areas within the SGL boundaries derived from the best performing SGL area-calculation technique. The application of Sneed and Hamilton's (2007) physically-based SGL depth-calculation algorithm to MODIS's red band predicts SGL depths and volumes in West Greenland with errors comparable to those in other studies (Pope et al., 2016). Using MODIS's red band instead of its green band produces significantly better results. There are two possible reasons for this. First, red light attenuates more strongly in the water column than green light, and can reproduce a range of water depths more reliably (Pope et al., 2016), particularly at shallower depths. Second, resolution sharpening applied to MODIS's green band (which is not required for the red band) likely results in loss of accuracy in surface-reflectance values, which then carry through into the SGL depth calculations. Although SGL depths and volumes calculated with MODIS's red band are dispersed around a linear regression line, producing low r values (Fig. 10; Tables 2 and 3), the derived RMSE values are low compared to depths and volumes generated from the green band (Tables 2 and 3). The RMSE of 1.27 m for SGL depth is higher than those for SGL depths derived for LS8's higher-resolution red (RMSE = 0.28 m) and panchromatic (RMSE = 0.63 m) bands (Pope et al., 2016), but is lower than values from other studies using empirically derived depth-reflectance techniques for MODIS imagery (e.g. RMSE = 1.47 m in Fitzpatrick et al. (2014)).

5.2.1. Underestimation of MODIS supraglacial lake depths and volumes

Despite the better performance of the physically-based SGL depth calculation algorithm using the red over the green band, using the red band still tends to produce lower MODIS SGL depths and volumes than those calculated from the LS8 data. This is likely due to the different spatial resolutions of the two datasets. LS8's higher resolution means that deep water towards SGL centres is reliably sampled as dark pixels. They will not be reliably sampled with MODIS's coarser resolution data if the shallower water depths away from the SGL centres bias MODIS pixels towards those shallower depths, which would then appear as relatively bright pixels. We attempt to correct for this when we compare LS8 and MODIS-derived SGL pixel depths by resampling the LS8 depth arrays (Section 3.4), but it is probable that this effect cannot be eliminated entirely. Furthermore, the lower MODIS SGL depths and volumes may also be explained by the error in the SGL outlines to which the SGL depth-retrieval algorithm is applied. If the SGL area-derivation algorithm results in inaccurately resolved SGL perimeters, it is probable that (i) shallow water at the edges of SGLs will be omitted from the MODIS SGL volume calculations; and (ii) the value for A_d, which is taken as the mean of the reflectance of the ring of pixels surrounding the SGL outline, will be lower than it should be, since this ring may include

Table 4
Variation in the errors (as measured by the RMSE) for water depths derived from MODIS imagery compared with the LS8-derived depths across all images from both study regions. n is the number of data points within each given range.

Depth range (m)	n	RMSE (m)
0.0–0.5	169	1.08
0.5–1.0	599	1.24
1.0–1.5	371	1.14
1.5–2.0	220	1.07
2.0–2.5	106	1.00
2.5–3.0	75	1.18
3.0–3.5	40	1.17
3.5–4.0	29	1.40
>4.0	55	2.99

Table 5
Variation in the errors (as measured by the RMSE) for SGL volumes derived from MODIS imagery compared with the LS8-derived volumes across all images from both study regions. n is the number of data points within each given range.

Volume range ($\times 10^7$ m^3)	n	RMSE ($\times 10^7$ m^3)
0.0–0.5	8	4.0
0.5–1.0	57	4.4
1.0–2.0	66	3.9
2.0–2.5	19	5.7
2.5–3.0	17	5.5
3.0–3.5	17	5.5
3.5–4.0	11	5.2
4.0–5.0	21	6.6
5.0–6.0	15	5.5
6.0–7.0	12	8.0
7.0–10.0	21	6.9
>10.0	24	10.8

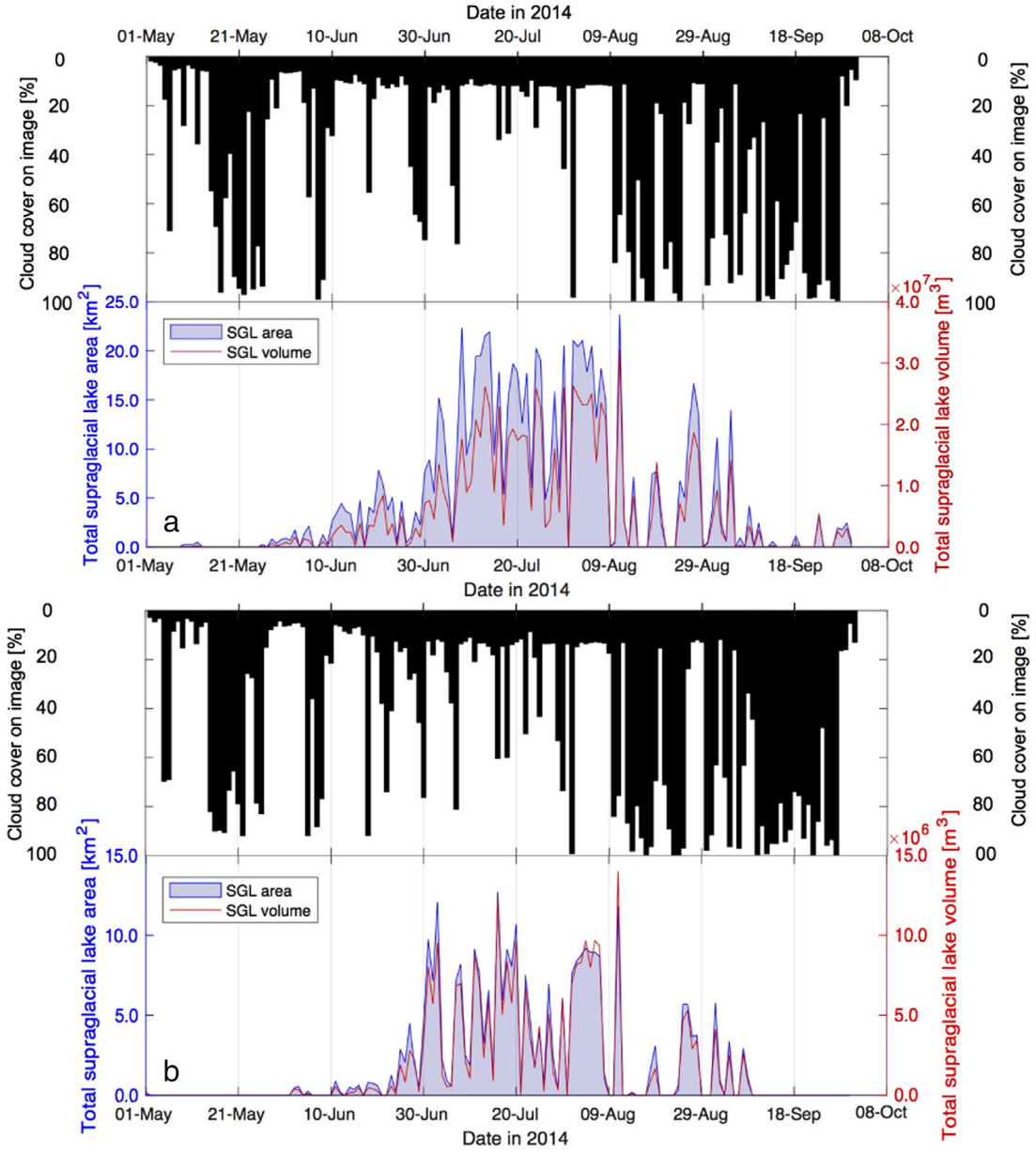

Fig. 11. Total SGL area, volume and percentage cloud cover for the (a) Paakitsoq and (b) Store Glacier regions during the 2014 melt season. The large mid-season decreases in total SGL area and volume to values that are at or close to zero correspond with high regional cover by clouds, explaining the seasonal pattern of anomalies in total SGL area and volume evolution.

some shallow water when it is intended to contain only bare ice. This error may be especially influential since the SGL depth-calculation algorithm is particularly sensitive to A_d values (Georgiou et al., 2009; Pope et al., 2016). Finally, the depth and volume validation data derived from LS8 have errors associated with them since they are also derived from the same physically-based SGL depth-retrieval algorithm. For example, LS8's red and panchromatic bands may not be able to accurately resolve the deepest (>4 m) water (Moussavi et al., 2016), which may explain our pattern of higher RMSEs at higher water depths (Table 4). Comparing the MODIS-derived depths with field data or very high-resolution DEM data (similar to Pope et al. (2016) or Moussavi et al. (2016)) would provide additional tests of the algorithm's performance beyond those reported here, and would be a valuable future study, particularly given the now freely available high-resolution Arctic DEM from the Polar Geospatial Center (http://pgc.umn.edu/arcticdem).

Scaling the MODIS SGL volumes using the slope coefficient from the linear regression line for the MODIS and LS8 SGL volume data produces only a marginal improvement to the SGL volume estimates, and given this is derived from a limited number of data points ($n = 288$), this MODIS-LS8 scaling relationship is not included in the FAST algorithm.

5.3. Supraglacial lake evolution at Paakitsoq and Store Glacier

This study's third aim was to incorporate the best performing SGL area- and depth-calculation techniques into a fully automated SGL tracking algorithm, allowing automatic SGL depth and volume calculations across regions of the GrIS. Our FAST algorithm permits additional insights into the GrIS's surface hydrology to be made compared with many previous studies in which only SGL areas were tracked between images. As might be expected, we find that total SGL volume scales with the number of SGLs on an image (Fig. 12(a) and (c)). However, we also find that the mean SGL size across an individual image does not change alongside the total number of SGLs present on the image (Fig. 12(b) and (d)). This suggests that as the melt season progresses, with more SGLs developing on the ice sheet, the total SGL water volume on an image increases by the presence of increasingly numerous SGLs

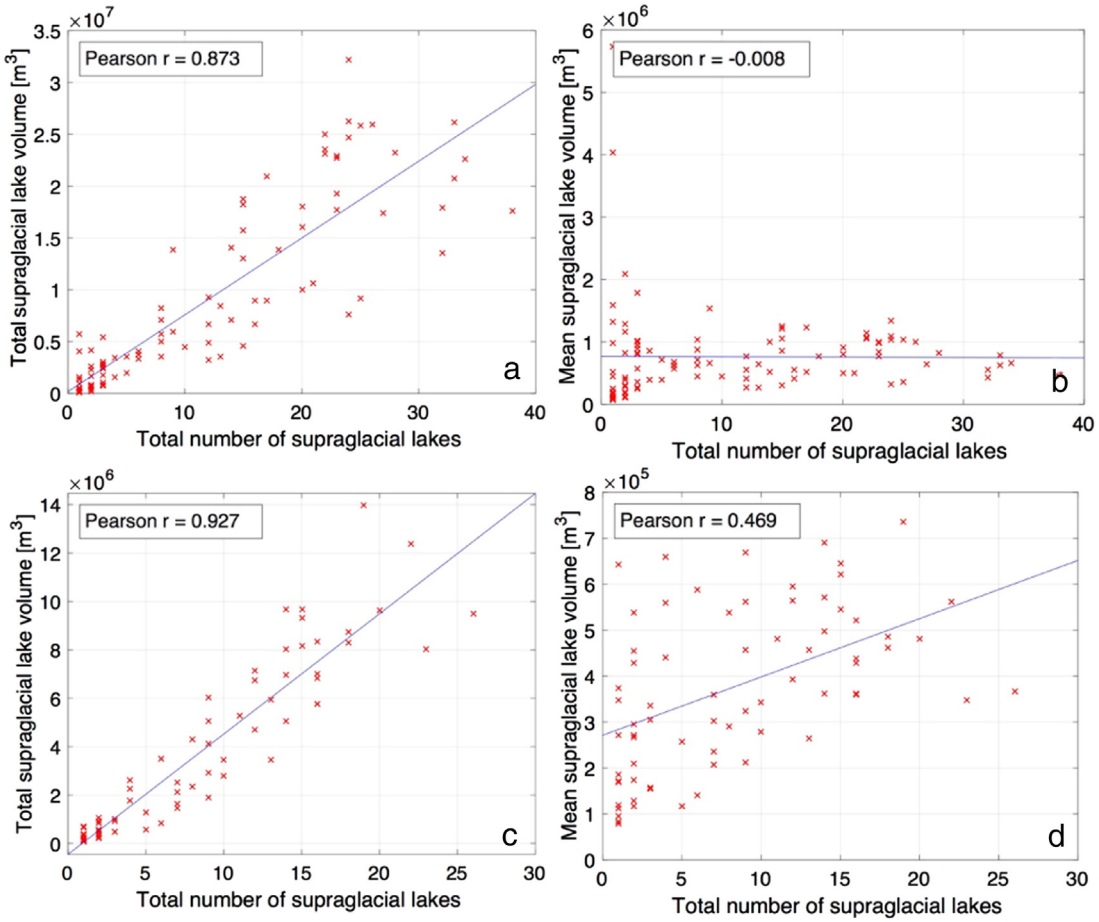

Fig. 12. The relationship between the total number of SGLs on each individual image in the season and the total and mean SGL water volume for each individual image. Note that images for which no SGLs were identified are not plotted. Subplots (a) and (b) show relationships for the Paakitsoq region, with (c) and (d) being for the Store Glacier region. The blue lines on all subplots display an ordinary least-squares linear regression. *r* values, derived from the Pearson product-moment correlation, are significant (p-value < 0.01) at the 99% confidence interval for subplots (a) and (c), but are not significant at the 95% confidence interval for subplots (b) and (d).

instead of through increases to the dimensions of individual SGLs. This might suggest an overall region-wide control on SGL volume, such as limits to the size of ice-surface topographic depressions, preventing the formation of larger SGLs. However, the slightly stronger relationship between mean SGL volume and the total number of SGLs on an image (Fig. 12(d)) at Store Glacier could indicate that this control is less dominant here than at Paakitsoq.

5.3.1. Rapidly draining supraglacial lakes

The final aim of our study was to use the FAST algorithm to examine the incidence of rapid SGL drainage across the two study regions in West Greenland. The numbers of rapidly draining SGLs, as a proportion of the total SGL population, identified by the FAST algorithm within the study regions (21% and 15% of the total SGL population at Paakitsoq and Store Glacier, respectively) are similar to results from other ice-marginal (i.e. <80 km inland) areas of West Greenland (e.g. the 28% at Russell Glacier reported by Fitzpatrick et al. (2014)). As the melt season progresses, there are increasing numbers of rapid drainage events at higher elevations (Fig. 13). This can be expected due to an upglacier increase in total meltwater production over the season, causing the filling of progressively higher SGLs to reach the water volume required to drain. Similarly, the lack of early-season rapid drainage events at high elevations is because there are few SGLs there. For example, during the 19 June to 28 June period, the single SGL within the 1200–1399 m elevation band drains rapidly; by the 8 August to 18 August period, only 10% of the SGLs within the same elevation band drain rapidly (Fig. 13). Fewer rapid events occur at lower surface elevations (<600 m) later in the season because most SGLs that could drain would have done so earlier in the season.

Among the rapidly draining SGLs identified by the FAST algorithm, we detect clusters of drainage events (which are defined as events that occur within four days and 10 km of each other), as was also observed by Fitzpatrick et al. (2014) at Russell Glacier. In the Paakitsoq region, three SGLs drain in mid-July at a similar elevation band and with comparable ice thicknesses beneath them; a similar pattern is observed for a SGL cluster in early July at Store Glacier (Figs. 5 and 14). In addition, one SGL at Paakitsoq drains twice within the season: once on 12 June and then again on 10 July (Fig. 5, yellow circle). This observation of the filling, drainage, re-filling and re-drainage of a SGL is a phenomenon that has been reported only once previously in a remote-sensing study (Fitzpatrick et al., 2014) and once in a field-based study (Brizgys and

Table 6
Summary of the results from the FAST algorithm applied to the two study sites. See Tables S4 and S5 for the full details of all of the rapid SGL drainage events within both regions.

Property	Paakitsoq region	Store Glacier region
Number of rapid drainage events	43	19
% SGLs draining rapidly	21	15
Median date of rapid drainage	12 July	7 July
Modal date of rapid drainage	13 July	3 July
Total water lost due to rapid drainage (m^3)	1.9×10^7	6.6×10^6
Mean water lost per rapid event (m^3)	4.3×10^5	3.5×10^5

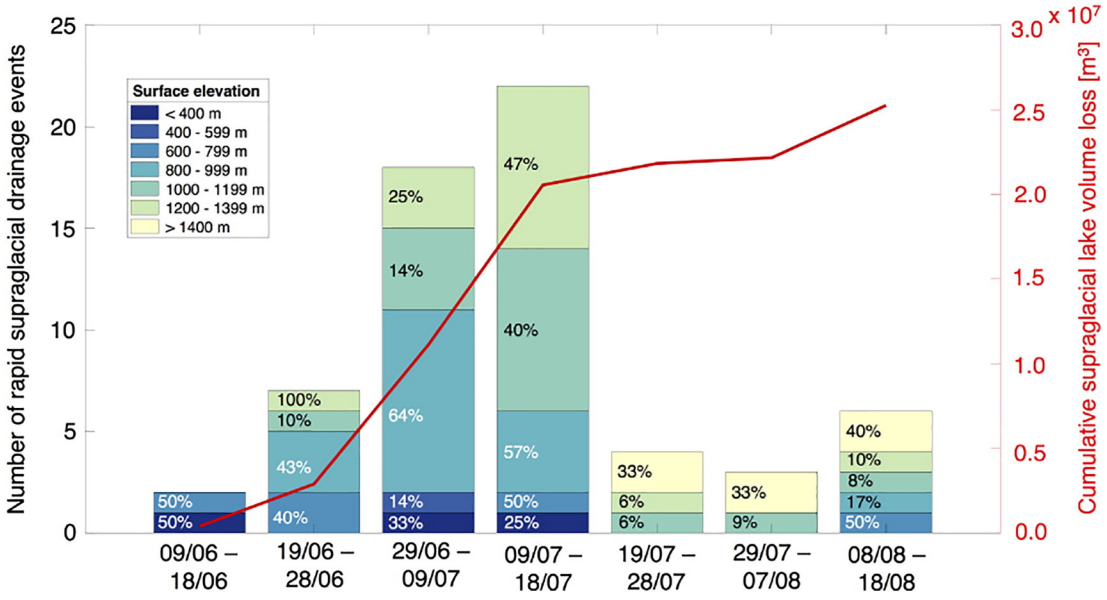

Fig. 13. The number of rapid SGL drainage events across both study sites, binned by initiation dates and stacked by surface elevation of SGLs' locations. Cumulative SGL volume loss from all rapid events in 2014 is shown by the solid red line. The percentage figures give the percentage of SGLs that drain within each elevation band relative to the maximum number of observed SGLs within that elevation band over the corresponding dates.

Box, 2005). It is encouraging that the FAST algorithm can automatically detect similar phenomena.

Given that the twice-draining SGL is found to reach a similar water volume before draining rapidly on two occasions ($2.2 \times 10^5 \pm 5.6 \times 10^7$ m^3 versus $2.1 \times 10^5 \pm 5.6 \times 10^7$ m^3), we investigate the idea of a critical water volume threshold related to local ice thickness to explain rapid drainage. However, we find no relationship between SGL water volume immediately prior to rapid drainage and the local ice thickness (Fig. 15), suggesting that a universal critical water volume threshold required to initiate hydrofracture, which is dependent solely on local ice thickness, does not exist across the GrIS. This is in line with the suggestion of previous workers that factors other than simply local ice thickness will determine the SGL water volume required to initiate hydrofracture and thus the rapid SGL drainage process (Banwell et al., 2013, 2016; Arnold et al., 2014; Fitzpatrick et al., 2014; Stevens et al., 2015). We also compare the water volumes immediately prior to rapid SGL drainage within our study regions against the water volume that is required to initiate rapid hydrofracture beneath SGLs identified by Krawczynski et al. (2009). They indicate that SGLs with diameters ≥ 0.25 km (equivalent to areas ≥ 0.0491 km^2 if approximated as perfect circles) overlying sub-freezing ice of 1000 m thickness can initiate hydrofracture. We scale this critical SGL area value to SGL volume using the area-volume scaling relationships identified for the two regions (Section 5.3.2). At Paakitsoq, all SGLs meet or exceed this threshold, but at Store Glacier, many SGLs drain with water volumes that are considerably below this threshold (Fig. 15). This again indicates that the application of a universal critical water-volume threshold across the two regions is unlikely to be a robust explanatory variable for the prediction of hydrofracture, suggesting that one or several other factors are also important.

5.3.2. Supraglacial lake area to volume scaling

Various studies have assumed that SGL volume is strongly correlated with SGL area in MODIS images and have established empirically-based SGL area to volume scaling relationships, either by using area as a proxy for volume (Box and Ski, 2007; Morriss et al., 2013), or by approximating SGL basins as cones with SGL area as the independent variable within a non-linear relationship (Liang et al., 2012). However, these studies lacked a high number of data points: for example, Box and Ski's (2007) area-volume scaling relationship ($R^2 = 0.620$; p-value < 0.01) was based on only 31 data points. Our study permits SGL area-to-volume scaling factors to be derived across the full melt season for the two regions of the GrIS, allowing us to test the validity of the relationships established in previous work. For Paakitsoq, we establish a SGL area-volume scaling relationship ($n = 1114$) using a quadratic least-squares regression (Fig. S1):

$$volume = 575341(area^2) + 271187(area) + 89617. \quad (3)$$

This SGL area-volume scaling basis is significantly stronger than an ordinary least-squares linear regression relationship ($R^2 = 0.827$; p-value < 0.01; RMSE = 0.420×10^6 m^3). At Store Glacier, we obtain a similarly strong relationship ($n = 558$) using an ordinary least-squares linear regression (Fig. S2):

$$volume = 1191332(area) - 161311. \quad (4)$$

Again, we observe a strong relationship ($R^2 = 0.869$; p < 0.01; RMSE = 0.184×10^6 m^3). Using a quadratic least-squares regression does not significantly improve the R^2 at Store Glacier, so we opt for the linear model.

This difference in the required regression model for the two regions likely results from the presence of shallower SGLs at Store Glacier, perhaps due to a regional surface-topography control that limits SGL depth. This could mean that for SGLs with larger areas (i.e. >2.5 km^2) at Store Glacier, the shallower depths can be better described with a linear relationship, whereas, at Paakitsoq, there is more scatter in the volume data for these higher SGL area values since the SGLs can become deeper. The low RMSE values for both regions are particularly encouraging given that SGL area can only be resolved to within 0.0625 km^2 (i.e. one MODIS pixel) across the two regions, yet the SGL volumes show relatively little spread for similar SGL area values. Overall, these relationships indicate that SGL area derived from MODIS imagery represents a valid proxy for volume, matching the findings of Morriss et al. (2013) who obtained a similarly high R^2.

6. Conclusions

SGLs on the GrIS are commonly investigated with satellite imagery, with the fine temporal resolution MODIS record providing a valuable

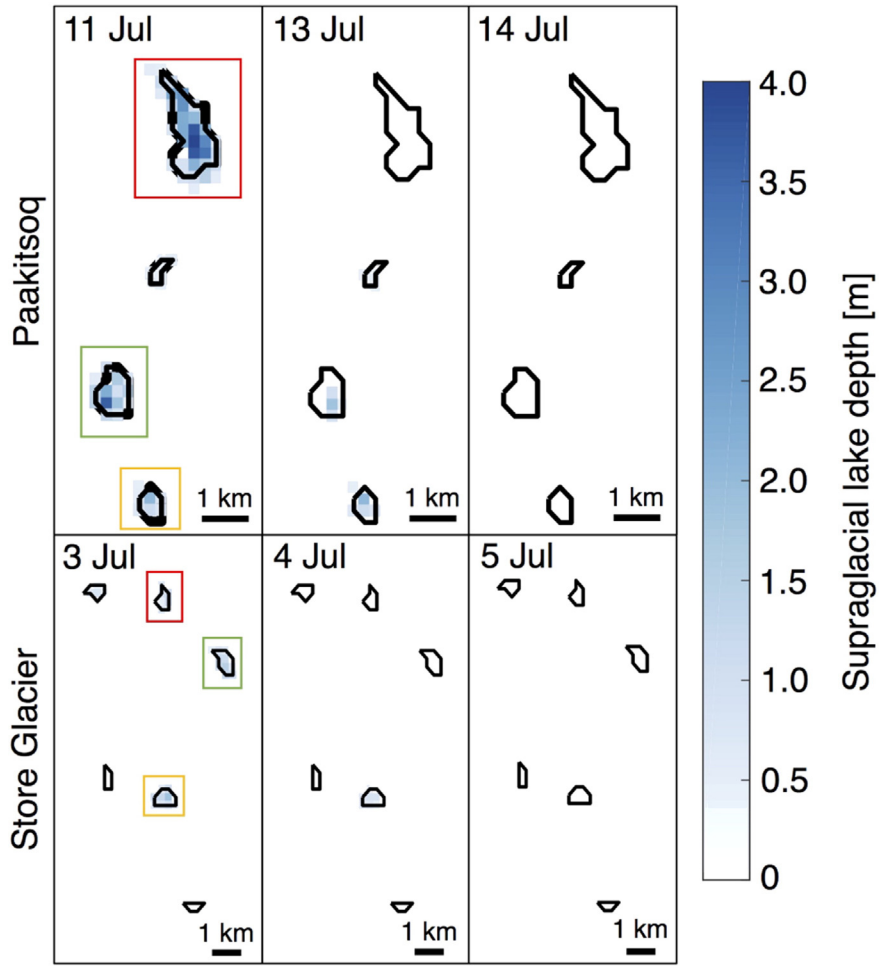

Fig. 14. Clusters of rapidly draining SGLs at Paakitsoq (top three panels) and Store Glacier (bottom three panels) identified by the FAST algorithm from MODIS imagery. The black outlines show the maximum extent of SGLs and represent the areas within which the FAST algorithm tracks changes to SGL area and volume over the full 2014 season. The area for Paakitsoq is equivalent to the area shown within the green box on Fig. 5(a) and the area for Store Glacier is equivalent to the area shown within the orange box on Fig. 5(b). For Paakitsoq, the SGL contained within the red box drains entirely between 11 July (coincident with its maximum water volume) and 13 July; the SGLs within the green and orange boxes drain entirely between 11 July (when they contain their maximum water volumes) and 14 July. For Store Glacier, the SGLs within the red and green boxes drain entirely between 3 July and 4 July, and the SGL within the orange box drains rapidly between 3 July and 5 July; these three SGLs contain their maximum water volumes on 3 July.

dataset since it has the potential to resolve dynamic changes to SGL areas and volumes over daily to weekly timescales. Many MODIS-based studies have derived SGL areas using semi- or fully automated approaches and then tracked the evolution of SGL areas across images; however, there has been little evaluation of the automatic methods used. Moreover, of the few studies that calculate both SGL depths and volumes from MODIS data, none have tracked volumes between images, and so no previous studies have systematically identified the locations, timings and quantified the volumes of water entering the GrIS's internal hydrological system via rapidly draining SGLs.

In this study, we have addressed these points through the development of a fully automated algorithm capable of tracking SGL areas and volumes between MODIS images, which we think is the most comprehensive SGL tracking algorithm to date. The FAST algorithm incorporates fully automatic (i) SGL area-derivation methods and (ii) physically-based SGL depth calculations. Both of these approaches do not rely upon field data for calibration, allowing for the widespread application of the FAST algorithm across the GrIS. To select the best approach for (i), and to address the first aim of the study, we evaluated three existing methods of deriving SGL areas, finding that dynamic thresholding applied to the MODIS red-band MOD09 surface-reflectance data, with a threshold value of 0.640, significantly outperformed other area-calculation methods, and could reproduce SGL areas with high accuracy when compared with LS8-derived areas and without threshold adjustment on a site- or lake-specific basis. Although SGLs < 0.125 km^2 cannot be resolved with MODIS imagery, they accounted for <18% of the total water-covered areas (as measured by MODIS) within both our study regions, justifying the exploitation of MODIS's high temporal resolution to investigate GrIS hydrology. For (ii), and to address the second aim of this study, we followed Sneed and Hamilton (2007) and found that the application of their method to MODIS's red band produced accurate SGL depths and volumes when compared with LS8-derived values (RMSE for depth: 1.27 m; RMSE for volume: 5.9×10^7 m^3). These errors are comparable to those produced using empirically-based depth-retrieval methods applied to MODIS imagery (Fitzpatrick et al., 2014). The SGL depth calculations were only slightly less accurate than those derived using the same physically-based algorithm applied to higher-resolution sensors, such as LS8: when comparing our RMSE for SGL depth against Pope et al.'s (2016) RMSEs, the difference is <1 m. To achieve the third and fourth aims of this study, we incorporated the best methods identified from the first two aims into the FAST algorithm, and then applied it to two study regions. Here, it successfully reproduced the expected patterns of SGL evolution, including the identification of 62 rapid drainage events, some drainage event clustering across both regions, and the drainage, refilling and re-drainage of one SGL in the Paakitsoq region. We found no

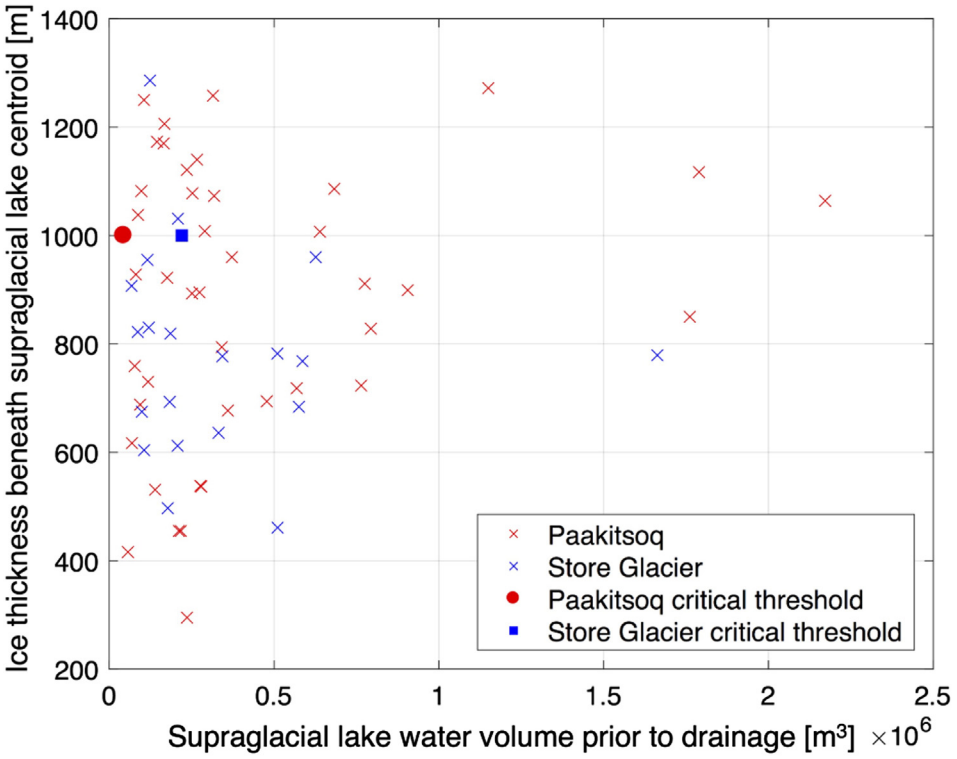

Fig. 15. Scatterplot of SGL water volumes immediately prior to drainage, and the ice thickness beneath SGL centroids, for the two study sites. For Paakitsoq: $R^2 = 0.03$; for Store Glacier: $R^2 = 0.00$. Both R^2 values are not significant at the 95% confidence interval. The critical SGL water volume thresholds required to initiate hydrofracture from Krawczynski et al. (2009) are also shown for the two regions.

statistically significant relationship between the rapidly draining SGL water volumes identified by the FAST algorithm and the local ice thickness beneath the SGLs. This indicates that factors other than the local ice thickness are likely to be important in controlling the SGL water volume required to initiate hydrofracture, in line with previous research (Arnold et al., 2014; Fitzpatrick et al., 2014; Stevens et al., 2015).

The FAST algorithm's main improvement on previous SGL tracking methods (e.g. Selmes et al., 2011; Liang et al., 2012) is its ability to calculate automatically SGL volumes and then to track them across wide swathes of the GrIS. Given this, the high temporal resolution of the MODIS record can now be fully exploited to significantly extend previous remotely based calculations of SGL depth and volume. Future work will generate outputs from the FAST algorithm to investigate the locations, timings and water volumes of rapid SGL drainage events at the whole GrIS scale. Such analysis should help to identify factors other than the local ice thickness that may control the volume of SGL water required to initiate hydrofracture. The SGL water volume data and the statistical relationships generated by these applications of the FAST algorithm may also inform the boundary conditions and validations of supraglacial hydrology models. Furthermore, the application of the FAST algorithm will allow water volumes reaching the subglacial drainage system across different regions, and in different years, to be calculated more effectively, which could help better explain the observed patterns of intra- and inter-annual ice-velocity variations, and also form a valuable additional input to ice-dynamic models. These applications and developments of the FAST algorithm are likely to permit greater insight into the GrIS's present and future hydrology, and thus its ongoing contribution to sea-level rise.

Data availability

The FAST algorithm presented in this study can be made available for use by others through contact with the corresponding author.

Acknowledgements

This research was funded by a UK Natural Environment Research Council PhD studentship awarded to A.G.W. through the Cambridge Earth System Science Doctoral Training Partnership (grant number: NE/L002507/1). A.F.B. acknowledges the support of a Bowring Junior Research Fellowship (St Catharine's College, University of Cambridge) and a Leverhulme/Newton Trust Early Career Fellowship. Valuable discussions with Nick Selmes and the contents of his doctoral thesis helped to develop ideas during the early stages of this research. We are grateful to Tom Chudley for suggesting the acronym for the FAST algorithm. Finally, we thank Allen Pope and one anonymous reviewer for their detailed comments that significantly improved the quality of this paper.

Appendix A. Supplementary data

Supplementary data to this article can be found online at http://dx.doi.org/10.1016/j.rse.2017.04.032.

References

Alley, R.B., Dupont, T.K., Parizek, B.R., Anandakrishnan, S., 2005. Access of surface meltwater to beds of sub-freezing glaciers: preliminary insights. Ann. Glaciol. 40:8–14. http://dx.doi.org/10.3189/172756405781813483.

Andrews, L.C., Catania, G.C., Hoffman, M.J., Gulley, J.D., Lüthi, M.P., Ryser, C., Hawley, R.L., Neumann, T.A., 2014. Direct observations of evolving subglacial drainage beneath the Greenland Ice Sheet. Nature 514:80–83. http://dx.doi.org/10.1038/nature13796.

Arnold, N.S., Banwell, A.F., Willis, I.C., 2014. High-resolution modelling of the seasonal evolution of surface water storage on the Greenland Ice Sheet. Cryosphere 8: 1149–1160. http://dx.doi.org/10.5194/tc-8-1149-2014.

Banwell, A.F., Arnold, N.S., Willis, I.C., Tedesco, M., Ahlstrøm, A.P., 2012. Modeling supraglacial water routing and lake filling on the Greenland Ice Sheet. J. Geophys. Res. 117, F04012. http://dx.doi.org/10.1029/2012JF002393.

Banwell, A.F., Willis, I.C., Arnold, N.S., 2013. Modeling subglacial water routing at Paakitsoq, W Greenland. J. Geophys. Res. Earth 118:1282–1295. http://dx.doi.org/10.1002/jgrf.20093.

Banwell, A.F., Caballero, M., Arnold, N.S., Glasser, N.F., Cathles, L.M., MacAyeal, D.R., 2014. Supraglacial lakes on the Larsen B ice shelf, Antarctica, and at Paakitsoq, West

Greenland: a comparative study. Ann. Glaciol. 55 (66). http://dx.doi.org/10.3189/2014AoG66A049.
Banwell, A., Hewitt, I., Willis, I., Arnold, N., 2016. Moulin density controls drainage development beneath the Greenland Ice Sheet. J. Geophys. Res. 121 (12):2248–2269. http://dx.doi.org/10.1002/2015JF003801.
Bartholomew, I., Nienow, P., Mair, D., Hubbard, A., King, M.A., Sole, A., 2010. Seasonal evolution of subglacial drainage and acceleration in a Greenland outlet glacier. Nat. Geosci. 3:408–411. http://dx.doi.org/10.1038/NGEO863.
Bartholomew, I.D., Nienow, P., Sole, A., Mair, D., Cowton, T., King, M.A., Palmer, S., 2011a. Seasonal variations in Greenland Ice Sheet motion: Inland extent and behaviour at higher elevations. Earth Planet. Sci. Lett. 307 (3–4):271–278. http://dx.doi.org/10.1016/j.epsl.2011.04.014.
Bartholomew, I.D., Nienow, P., Sole, A., Mair, D., Cowton, T., Palmer, S., Wadham, J., 2011b. Supraglacial forcing of subglacial drainage in the ablation zone of the Greenland Ice Sheet. Geophys. Res. Lett. 38, L08502. http://dx.doi.org/10.1029/2011GL047063.
Bartholomew, I., Nienow, P., Sole, A., Mair, T., Cowton, T., King, M.A., 2012. Short-term variability in Greenland Ice Sheet motion forced by time-varying meltwater drainage: implications for the relationship between subglacial drainage system behaviour and ice velocity. J. Geophys. Res. 117, F03002. http://dx.doi.org/10.1029/2011JF002220.
Bougamont, M., Christoffersen, P., Hubbard, A.L., Fitzpatrick, A.A., Doyle, S.H., Carter, S.P., 2014. Sensitive response of the Greenland Ice Sheet to surface melt drainage over a soft bed. Nat. Commun. 5 (5052). http://dx.doi.org/10.1038/ncomms6052.
Box, J.E., Ski, K., 2007. Remote sounding of Greenland supraglacial melt lakes: implications for subglacial hydraulics. J. Glaciol. 53 (181):257–265. http://dx.doi.org/10.3189/172756507782202883.
Brizgys, G., Box, J.E., 2005. West Greenland ice sheet melt lake observations and modeling. Eos Trans. Am. Geophys. Union (AGU) 86 (Fall Meeting Supplement, Abstract C41A-07).
Catania, G.A., Neumann, T.A., Price, S.F., 2008. Characterizing englacial drainage in the ablation zone of the Greenland ice sheet. J. Glaciol. 54 (187), 567–578.
Colgan, W., Rajaram, H., Anderson, R., Steffen, K., Phillips, T., Joughin, I., Zwally, H.J., Abdalati, W., 2011a. The annual glaciohydrology cycle in the ablation zone of the Greenland ice sheet: Part 1. Hydrology model. J. Glaciol. 57 (204):697–709. http://dx.doi.org/10.3189/002214311797409668.
Colgan, W., Steffen, K., McLamb, W.S., Abdalati, W., Rajaram, H., Motyka, R., Phillips, T., Anderson, R., 2011b. An increase in crevasse extent, West Greenland: hydrologic implications. Geophys. Res. Lett. 38, L18502. http://dx.doi.org/10.1029/2011GL048491.
Cowton, T., Nienow, P., Sole, A., Wadham, J., Lis, G., Bartholomew, I., Mair, D., Chandler, D., 2013. Evolution of drainage system morphology at a land-terminating Greenlandic outlet glacier. J. Geophys. Res. Earth 118:29–41. http://dx.doi.org/10.1029/2012JF002540.
Das, S.B., Joughin, I., Behn, M.D., Howat, I.M., King, M.A., Lizarralde, D., Bhatia, M.P., 2008. Fracture propagation to the base of the Greenland Ice Sheet during supraglacial lake drainage. Science 320 (5877):778–781. http://dx.doi.org/10.1126/science.1153360.
Dow, C.F., Kulessa, B., Rutt, I.C., Tsai, V.C., Pimentel, S., Doyle, S.H., van As, D., Lindbäck, K., Pettersson, R., Jones, G.A., Hubbard, A., 2015. Modeling of subglacial hydrological development following rapid supraglacial lake drainage. J. Geophys. Res. Earth 120:1127–1147. http://dx.doi.org/10.1002/2014JF003333.
Doyle, S.H., Hubbard, A.L., Dow, C.F., Jones, G.A., Fitzpatrick, A., Gusmeroli, A., Kulessa, B., Lindback, K., Pettersson, R., Box, J.E., 2013. Ice tectonic deformation during the rapid in situ drainage of a supraglacial lake on the Greenland Ice Sheet. Cryosphere 7:129–140. http://dx.doi.org/10.5194/tc-7-129-2013.
Doyle, S.H., Hubbard, A., Fitzpatrick, A.A.W., van As, D., Mikkelsen, A.B., Pettersson, R., Hubbard, B., 2014. Persistent flow acceleration within the interior of the Greenland ice sheet. Geophys. Res. Lett. 41:899–905. http://dx.doi.org/10.1002/2013GL058933.
Everett, A., Murray, T., Selmes, N., Rutt, I.C., Luckman, A., James, T.D., Clason, C., O'Leary, M., Karunarathna, H., Moloney, V., Reeve, D.E., 2016. Annual down-glacier drainage of lakes and water-filled crevasses at Helheim Glacier, south east Greenland. J. Geophys. Res. Earth 121:1819–1833. http://dx.doi.org/10.1002/2016JF003831.
Fitzpatrick, A.A.W., Hubbard, A.L., Box, J.E., Quincey, D.J., van As, D., Mikkelsen, A.P.B., Doyle, S.H., Dow, C.F., Hasholt, B., Jones, G.A., 2014. A decade (2002—2012) of supraglacial lake volume estimates across Russell Glacier, West Greenland. Cryosphere 8:107–121. http://dx.doi.org/10.5194/tc-8-107-2014.
Fried, M.J., Catania, G.A., Bartholomaus, T.C., Duncan, D., Davis, M., Stearns, L.A., Nash, J., Shroyer, E., Sutherland, D., 2015. Distributed subglacial discharge drives significant submarine melt at a Greenland tidewater glacier. Geophys. Res. Lett. 42:9328–9336. http://dx.doi.org/10.1002/2015GL065806.
Gardelle, J., Arnaud, Y., Berthier, E., 2011. Contrasted evolution of glacial lakes along the Hindu Kush Himalaya mountain range between 1990 and 2009. Glob. Planet. Chang. 75 (1–2):47–55. http://dx.doi.org/10.106/j.gloplacha.2010.10.003.
Georgiou, S., Shepherd, A., McMillan, M., Nienow, P., 2009. Seasonal evolution of supraglacial lake volume from ASTER imagery. Ann. Glaciol. 50 (52):95–100. http://dx.doi.org/10.3189/172756409789624328.
Gumley, L., Descloitres, J., Schmaltz, J., 2007. Creating Reprojected True Color MODIS Images: A Tutorial, Version 1.0.2. University of Wisconsin-Madison and NASA Goddard Space Flight Center.
Hoffman, M.J., Catania, G.A., Neumann, T.A., Andrews, L.C., Rumrill, J.A., 2011. Links between acceleration, melting, and supraglacial lake drainage of the western Greenland Ice Sheet. J. Geophys. Res. 116, F04035. http://dx.doi.org/10.1029/2010JF001934.
Howat, I.M., de la Peña, S., van Angelen, J.H., Lenaerts, J.T.M., van den Broeke, M.R., 2013. Brief communication: expansion of meltwater lakes on the Greenland Ice Sheet. Cryosphere 7:201–204. http://dx.doi.org/10.5194/tc-7-201-2013.
Howat, I.M., Negrete, A., Smith, B.E., 2014. The Greenland Ice Mapping Project (GIMP) land classification and surface elevation datasets. Cryosphere 8:1509–1518. http://dx.doi.org/10.5194/tc-8-1509-2014.
Huggel, C., Kääb, A., Haeberli, W., Teysseire, P., Paul, F., 2002. Remote sensing based assessment of hazards from glacier lake outbursts: a case study in the Swiss Alps. Can. Geotech. J. 39 (2):316–330. http://dx.doi.org/10.1139/T01-099.
Ignéczi, A., Sole, A.J., Livingstone, S.J., Leeson, A.A., Fettweis, X., Selmes, N., Gourmelen, N., Briggs, K., 2016. Northeast sector of the Greenland Ice Sheet to undergo the greatest inland expansion of supraglacial lakes during the 21st century. Geophys. Res. Lett. 43. http://dx.doi.org/10.1002/2016GL070338.
Johansson, A.M., Brown, I.A., 2013. Adaptive classification of supra-glacial lakes on the West Greenland Ice Sheet. IEEE J. Sel. Top. Appl. Earth Obs. Remote Sens. 6 (4):1998–2007. http://dx.doi.org/10.1109/JSTARS.2012.2233722.
Johansson, A.M., Jansson, P., Brown, I.A., 2013. Spatial and temporal variations in lakes on the Greenland Ice Sheet. J. Hydrol. 476:314–320. http://dx.doi.org/10.1016/j.jhydrol.2012.10.045.
Joughin, I., Das, S.B., Flowers, G.E., Behn, M.D., Alley, R.B., King, M.A., Smith, B.E., Bamber, J., van den Broeke, M.R., van Angelen, J.H., 2013. Influence of ice-sheet geometry and supraglacial lakes on seasonal ice-flow variability. Cryosphere 7:1185–1192. http://dx.doi.org/10.5194/tc-7-1185-2013.
Krawczynski, M.J., Behn, M.D., Das, S.B., Joughin, I., 2009. Constraints on the lake volume required for hydro-fracture through ice sheets. Geophys. Res. Lett. 36, L10501. http://dx.doi.org/10.1029/2008GL036765.
Lampkin, D.J., 2011. Supraglacial lake spatial structure in western Greenland during the 2007 ablation season. J. Geophys. Res. Earth 116, F04001. http://dx.doi.org/10.1029/2010JF001725.
Lampkin, D.J., VanderBerg, J., 2011. A preliminary investigation of the influence of basal and surface topography on supraglacial lake distribution near Jakobshavn Isbrae, western Greenland. Hydrol. Process. 25:3347–3355. http://dx.doi.org/10.1002/hyp.8170.
Langley, E.S., Leeson, A.A., Stokes, C.R., Jamieson, S.S.R., 2016. Seasonal evolution of supraglacial lakes on an East Antarctic outlet glacier. Geophys. Res. Lett. 43:8563–8571. http://dx.doi.org/10.1002/2016GL069511.
Leeson, A.A., Shepherd, A., Sundal, A.V., Johansson, A.M., Selmes, N., Briggs, K., Hogg, A.E., Fettweis, X., 2013. A comparison of supraglacial lake observations derived from MODIS imagery at the western margin of the Greenland ice sheet. J. Glaciol. 59 (218):1179–1188. http://dx.doi.org/10.3189/2013JoG13J064.
Legleiter, C.J., Tedesco, M., Smith, L.C., Behar, A.E., Overstreet, B.T., 2014. Mapping the bathymetry of supraglacial lakes and streams on the Greenland ice sheet using field measurements and high-resolution satellite images. Cryosphere 8:215–228. http://dx.doi.org/10.5194/tc-8-215-2014.
Lettang, F.J., Crocker, R.I., Emery, W.J., Maslanik, J.A., 2013. Estimating the extent of drained supraglacial lakes on the Greenland Ice Sheet. Int. J. Remote Sens. 34 (13):4754–4768. http://dx.doi.org/10.1080/01431161.2013.782118.
Liang, Y., Colgan, W., Lv, Q., Steffen, K., Abdalati, W., Stroeve, J., Gallaher, D., Bayou, N., 2012. A decadal investigation of supraglacial lakes in West Greenland using a fully automatic detection and tracking algorithm. Remote Sens. Environ. 123:127–138. http://dx.doi.org/10.1016/j.rse.2012.03.020.
Lüthje, M., Pedersen, L.T., Reeh, N., Gruell, W., 2006. Modelling the evolution of supra-glacial lakes on the western Greenland ice sheet margin. J. Glaciol. 52 (179):608–618. http://dx.doi.org/10.3189/172756506781828386.
McMillan, M., Nienow, P., Shepherd, A., Benham, T., Sole, A., 2007. Seasonal evolution of supra-glacial lakes on the Greenland Ice Sheet. Earth Planet. Sci. Lett. 262 (3–4):484–492. http://dx.doi.org/10.1016/j.epsl.2007.08.002.
Miles, V.V., Miles, M.W., Johannessen, O.M., 2016. Satellite archives reveal abrupt changes in behavior of Helheim Glacier, southeast Greenland. J. Glaciol. 62 (231):137–146. http://dx.doi.org/10.1017/jog.2016.24.
Miles, E.S., Willis, I.C., Arnold, N.S., Steiner, J.F., Pellicciotti, F., 2017. Spatial, seasonal and interannual variability of supraglacial ponds in the Langtang Valley of Nepal, 1999 to 2013. J. Glaciol. 63 (237):88–105. http://dx.doi.org/10.1017/jog.2016.120.
Miles, K.E., Willis, I.C., Benedek, C.L., Williamson, A.G. and Tedesco, M., Towards monitoring surface and subsurface lakes on the Greenland Ice Sheet using Sentinel-1 SAR and Landsat-8 OLI imagery. Front. Earth Sci. (in review)
Morlighem, M., Rignot, E., Mouginot, J., Seroussi, H., Larour, E., 2014. Deeply incised submarine glacial valleys beneath the Greenland Ice Sheet. Nat. Geosci. 7:418–422. http://dx.doi.org/10.1038/NGEO2167.
Morriss, B.F., Hawley, R.L., Chipman, J.W., Andrews, L.C., Catania, G.A., Hoffman, M.J., Lüthi, M.P., Neumann, T.A., 2013. A ten-year record of supraglacial lake evolution and rapid drainage in West Greenland using an automated processing algorithm for multispectral imagery. Cryosphere 7:1869–1877. http://dx.doi.org/10.5194/tc-7-1869-2013.
Moussavi, M.S., Abdalati, W., Pope, A., Scambos, T., Tedesco, M., MacFerrin, M., Grigsby, S., 2016. Derivation and validation of supraglacial lake volumes on the Greenland Ice Sheet from high-resolution satellite imagery. Remote Sens. Environ. 183:294–303. http://dx.doi.org/10.1016/j.rse.2016.05.024.
Noël, B., van de Berg, W.J., Machguth, H., Lhermitte, S., Howat, I., Fettweis, X., van den Broeke, M.R., 2016. A daily, 1-km resolution data set of downscaled Greenland ice sheet mass balance (1958–2015). Cryosphere 10:2361–2377. http://dx.doi.org/10.5194/tc-10-2361-2016.
Palmer, S., Shepherd, A., Nienow, P., Joughin, I., 2011. Seasonal speedup of the Greenland Ice Sheet linked to routing of surface water. Earth Planet. Sci. Lett. 302:423–428. http://dx.doi.org/10.1016/j.epsl.2010.12.037.
Pope, A., 2016. Reproducibly estimating and evaluating supraglacial lake depth with Landsat 8 and other multispectral sensors. Earth Space Sci. 3:176–188. http://dx.doi.org/10.1002/2015EA000125.
Pope, A., Scambos, T.A., Moussavi, M., Tedesco, M., Willis, M., Shean, D., Grigsby, S., 2016. Estimating supraglacial lake depth in West Greenland using Landsat 8 and comparison with other multispectral methods. Cryosphere 10:15–27. http://dx.doi.org/10.5194/tc-10-15-2016.

Rignot, E., Velicogna, I., van den Broeke, M.R., Monaghan, A., Lenaerts, J.T.M., 2011. Acceleration of the contribution of the Greenland and Antarctic ice sheets to sea level rise. Geophys. Res. Lett. 38, L05503. http://dx.doi.org/10.1029/2011GL046583.

Ryan, J.C., Hubbard, A.L., Box, J.E., Todd, J., Christoffersen, P., Carr, J.R., Holt, T.O., Snooke, N., 2015. UAV photogrammetry and structure from motion to assess calving dynamics at Store Glacier, a large outlet draining the Greenland ice sheet. Cryosphere 9:1–11. http://dx.doi.org/10.5194/tc-9-1-2015.

Schoof, C., 2010. Ice-sheet acceleration driven by melt supply variability. Nature 468 (7325):803–806. http://dx.doi.org/10.1038/nature09618.

Selmes, N., 2011. Remote sensing of supraglacial lakes on the Greenland Ice Sheet. (Unpublished Ph.D. thesis). Department of Geography, Swansea University, Swansea, UK.

Selmes, N., Murray, T., James, T.D., 2011. Fast draining lakes on the Greenland Ice Sheet. Geophys. Res. Lett. 38, L15501. http://dx.doi.org/10.1029/2011GL047872.

Selmes, N., Murray, T., James, T.D., 2013. Characterizing supraglacial lake drainage on the Greenland Ice Sheet. Cryosphere Discuss. 7:475–505. http://dx.doi.org/10.5194/tcd-7-475-2013.

Shepherd, A., Hubbard, A., Nienow, P., King, M., McMillan, M., Joughin, I., 2009. Greenland ice sheet motion coupled with daily melting in late summer. Geophys. Res. Lett. 36, L01501. http://dx.doi.org/10.1029/2008GL035758.

Sneed, W.A., Hamilton, G.S., 2007. Evolution of melt pond volume on the surface of the Greenland Ice Sheet. Geophys. Res. Lett. 34, L03501. http://dx.doi.org/10.1029/2006GL028697.

Sole, A., Nienow, P., Bartholomew, I., Mair, D., Cowton, T., Tedstone, A., King, M.A., 2013. Winter motion mediates dynamic response of the Greenland Ice Sheet to warmer summers. Geophys. Res. Lett. 40:3940–3944. http://dx.doi.org/10.1002/grl.50764.

Stevens, L.A., Behn, M.D., McGuire, J.J., Das, S.B., Joughin, I., Herring, T., Shean, D.E., King, M.A., 2015. Greenland supraglacial lake drainages triggered by hydrologically induced basal slip. Nature 522:73–76. http://dx.doi.org/10.1038/nature14480.

Sundal, A., Shepherd, A., Nienow, P., Hanna, E., Palmer, S., Huybrechts, P., 2009. Evolution of supra-glacial lakes across the Greenland Ice Sheet. Remote Sens. Environ. 113: 2164–2171. http://dx.doi.org/10.1016/j.rse.2009.05.018.

Sundal, A.V., Shepherd, A., Nienow, P., Hanna, E., Palmer, S., Huybrechts, P., 2011. Melt-induced speed-up of the Greenland ice sheet offset by efficient sub-glacial drainage. Nature 469 (7331):521–524. http://dx.doi.org/10.1038/nature09740.

Tedesco, M., Steiner, S., 2011. In-situ multispectral and bathymetric measurements over a supraglacial lake in western Greenland using a remotely controlled watercraft. Cryosphere 5:445–452. http://dx.doi.org/10.5194/tc-5-445-2011.

Tedesco, M., Lüthje, M., Steffen, K., Steiner, N., Fettweis, X., Willis, I., Bayou, N., Banwell, A., 2012. Measurement and modeling of ablation of the bottom of supraglacial lakes in western Greenland. Geophys. Res. Lett. 39, L02502. http://dx.doi.org/10.1029/2011GL049882.

Tedesco, M., Willis, I.C., Hoffman, M.J., Banwell, A.F., Alexander, P., Arnold, N.S., 2013. Ice dynamic response to two modes of surface lake drainage on the Greenland ice sheet. Environ. Res. Lett. 8, 034007. http://dx.doi.org/10.1088/1748-9326/8/3/034007.

Tedstone, A.J., Nienow, P.W., Sole, A.J., Mair, D.W.F., Cowton, T.R., Bartholomew, I.D., King, M.A., 2013. Greenland ice sheet motion insensitive to exceptional melt water forcing. Proc. Natl. Acad. Sci. 110 (49):19719–19724. http://dx.doi.org/10.1073/pnas.1315843110.

Tedstone, A.J., Nienow, P.W., Gourmelen, N., Sole, A.J., 2014. Greenland ice sheet annual motion insensitive to spatial variations in subglacial hydraulic structure. Geophys. Res. Lett. 41:8910–8917. http://dx.doi.org/10.1002/2014GL062386.

Todd, J., Christoffersen, P., 2014. Are seasonal calving dynamics forced by buttressing from ice mélange or undercutting by melting? Outcomes from full-Stokes simulations of Store Glacier, West Greenland. Cryosphere 8:2353–2365. http://dx.doi.org/10.5194/tc-8-2353-2014.

USGS, 2013. Using the USGS Landsat 8 product.Available at:. http://landsat.usgs.gov/Landsat8_Using_Product.php (Accessed 20 September, 2016).

van den Broeke, M.R., Enderlin, E.M., Howat, I.M., Kuipers Munneke, P., Noël, B.P., van de Berg, W.J., van Meijgaard, E., Wouters, B., 2016. On the recent contribution of the Greenland ice sheet to sea level change. Cryosphere 10:1933–1946. http://dx.doi.org/10.5194/tc-10-1933-2016.

Vaughan, D.G., Cosimo, J.C., Allison, I., Carrasco, J., Kaser, G., Kwok, R., Mote, P., Murray, T., Paul, F., Ren, J., Rignot, E., Solomina, O., Steffen, K., Zhang, T., 2013. Observations: cryosphere. In: Stocker, T.F., Qin, D., Plattner, G.-K., Tignor, M., Allen, S.K., Boschung, J., Nauels, A., Xia, Y., Bex, V., Midgley, P.M. (Eds.), Climate Change 2013: The Physical Science Basis. Contribution of Working Group I to the Fifth Assessment Report of the Intergovernmental Panel on Climate Change. Cambridge University Press, Cambridge, United Kingdom and New York, NY, USA.

Xu, H., 2006. Modification of normalised difference water index (NDWI) to enhance open water features in remotely sensed imagery. Int. J. Remote Sens. 27 (14):3025–3033. http://dx.doi.org/10.1080/01431160600589179.

Yang, K., Smith, L.C., 2013. Supraglacial streams on the Greenland Ice Sheet delineated from combined spectral-shape information in high-resolution satellite imagery. IEEE Geosci. Remote Sens. Lett. 10 (4):801–805. http://dx.doi.org/10.1109/LGRS.2012.2224316.

Yang, K., Smith, L.C., 2016. Internally drained catchments dominate supraglacial hydrology of the southwest Greenland Ice Sheet. J. Geophys. Res. Earth 121:1891–1910. http://dx.doi.org/10.1002/2016JF003927.

Yang, K., Smith, L.C., Chu, V.W., Gleason, C.J., Li, M., 2015. A caution on the use of surface digital elevation models to simulation supraglacial hydrology of the Greenland Ice Sheet. IEEE J. Sel. Top. Appl. Earth Obs. Remote Sens. 8 (11):5212–5224. http://dx.doi.org/10.1109/JSTARS.2015.2483483.

Zwally, H.J., Abdalati, W., Herring, T., Larson, K., Saba, J., Steffen, K., 2002. Surface melt-induced acceleration of Greenland ice-sheet flow. Science 297 (5579):218–222. http://dx.doi.org/10.1126/science.107270.